Clemson University
TigerPrints

All Theses | Theses

5-2024

Mechanical and Thermal Measurement Techniques for Crystalline-Core/Crystalline-Clad Optical Fibers

Evan Watkins
ewatki4@clemson.edu

Follow this and additional works at: https://tigerprints.clemson.edu/all_theses

 Part of the Condensed Matter Physics Commons

Recommended Citation

Watkins, Evan, "Mechanical and Thermal Measurement Techniques for Crystalline-Core/Crystalline-Clad Optical Fibers" (2024). *All Theses*. 4293.
https://tigerprints.clemson.edu/all_theses/4293

This Thesis is brought to you for free and open access by the Theses at TigerPrints. It has been accepted for inclusion in All Theses by an authorized administrator of TigerPrints. For more information, please contact kokeefe@clemson.edu.

Mechanical and Thermal Measurement Techniques for Crystalline-Core/Crystalline-Clad Optical Fibers

---

A Thesis
Presented to
the Graduate School of
Clemson University

In Partial Fulfillment
of the Requirements for the Degree
Masters of Science
Physics

---

by
Evan Douglas Watkins
May 2024

Accepted by:
Dr. Apparao M. Rao, Committee Chair
Dr. Bradley S. Meyer
Dr. Sumanta Tewari

Abstract

Optical fiber laser systems offer advantages such as high optical gain, efficient cooling, and the production of high-quality optical beams. Fiber lasers are characterized by their unique core-cladding structure, providing optical benefits and mechanical properties that impact their performance. Interests in materials such as yttrium aluminum garnets (YAG) and lutetium oxide (Lu_2O_3 also lutetia) as laser mediums are due to their high average power capabilities, but thermal management remains a challenge. This thesis discusses the choice of ytterbium (Yb^{3+}) as a dopant in YAG and lutetia, exploring its electronic structure and relevance to thermal properties. The thesis focuses on the development and implementation of optical fiber bend tests and thermal conductivity measurement techniques on reference materials. Mechanical properties can be evaluated using two-, three-, and four-point bend tests however a four-point bend model is introduced to investigate the mechanical effects of cladding. The parallel thermal conductance and optothermal Raman techniques are explored and tested with reference samples in order to use them to measure the thermal conductivity of optical fiber systems in future work.

Dedication

To my father, Douglas,
for his leveled guidance.

To my mother, Anna,
for her unwavering support.

To my love, 김도연,
who gives life new meaning.

Acknowledgments

I would like to express my gratitude to my advisor, Dr. Apparao M. Rao, for the opportunities he has provided. I am thankful to my committee members, Dr. Bradley S. Meyer and Dr. Sumanta Tewari, for their valuable time and service on my committee. Additionally, I thank my CNI research team members, the Physics and Astronomy Instrument Shop, Dr. Rahul Rao at the Wright Patterson Air Force Base. This work was supported through the US Army Space and Missile Defense Command (SMDC) Award/Contract No. W9113M22D0061. This work was also partly supported by the R. A. Bowen Fellowship funds in the College of Science, and the data presented herein was obtained at the Clemson Nanomaterials Institute, which Clemson University operates.

Contents

List of Figures

Chapter 1

Introduction to Fiber Lasers

Since the first application of neodymium-doped glass for fiber lasers in 1964 [1], fiber lasers have garnered significant interest from researchers for various applications, including military [2] and scientific research. Fiber lasers offer many potential benefits over traditional solid-state lasers due to their high optical gain, efficient cooling, and the generation of high-quality optical beams, among other properties [3–5]. Fiber lasers are unique in their design and characterized by a distinct structure. They typically comprise an active medium (a source of optical gain from stimulated emission) in a cylindrical core surrounded by a carefully chosen coating called a cladding. This core-cladding design (Figure 1.1) offers various optical advantages, such as total internal reflection, numerical aperture tuning, and even the possibility of multi-mode operation. Additionally, the cladding can alter the mechanical properties of the optical fiber, which, in some cases, can enhance flexibility or induce fragility. However, the exceptional beam quality and reliability of fiber lasers have positioned them as a key technology in modern photonics, enabling precise and versatile laser systems that continue to push the boundaries of what is achievable in optics and laser technology. However, a crucial aspect of fiber lasers is their distinctive core-cladding fabrication

and its impact on thermal and mechanical properties.

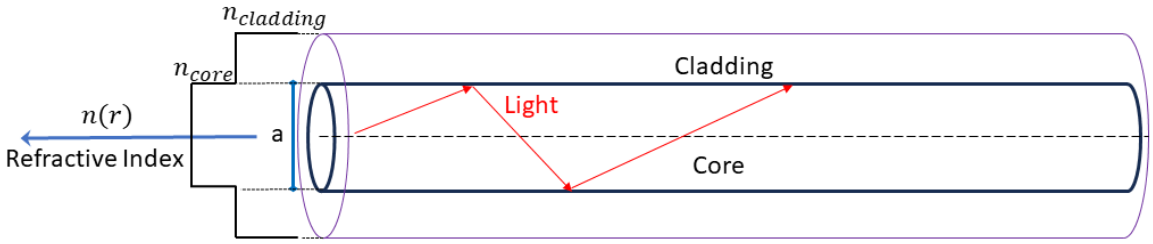

Figure 1.1: Schematic of a clad-core optical fiber designed for total internal reflection

Recently, there has been a growing interest in yttrium aluminum garnets (YAG) and lutetium oxide (Lu_2O_3, also known as lutetia) as active laser media. This increased attention is attributed mainly to their remarkable ability to operate at high average powers [6–8]. However, it's essential to note that managing thermal issues remains a critical and recurring challenge in high-power laser systems. The intense pumping process generates substantial latent heat, primarily from inherent quantum defects, leading to non-radiative transitions during the energy conversion. A quantum defect describes the difference in energy of a pump photon with that of a signal photon (the photon in the output radiation). The energy difference is dissipated as heat. Currently, these systems are thermally constrained in their power scaling limits [6, 9], which entails increasing power output without compromising the fiber's optical properties. Efficiently managing this heat is imperative for maintaining the performance and reliability of high-power lasers. Without effective thermal control, excessive heat can lead to various issues, including thermal lensing, coatings damage, and laser gain medium degradation. To prevent these detrimental effects and ensure the longevity and consistent operation of high-power lasers, meticulous thermal management and high mechanical stress resistance are fundamental in their design and operation. YAG and lutetia emerge as appealing candidates in this re-

gard, primarily because of their exceptional high-power scaling limits, attributed to their remarkable thermal conductivity, which efficiently dissipates the heat generated [10]. Consequently, they can scale to power levels of ∼40 and 47 kilowatts (kW), respectively [9].

YAG and lutetia may indeed have high thermal conductivities; however, these crystals are often doped with rare earth metals such as neodymium (Nd), chromium (Cr), erbium (Er), thulium (Tm), or ytterbium (Yb). Introducing dopants alters the crystal structure, lowering the material's thermal conductivity. This occurs mainly due to the ion size mismatch between the dopant and the host lattice ions, leading to lattice strain and phonon scattering from mass fluctuations. However, dopants offer numerous advantages to laser systems, including improved gain (light amplification), broadened wavelength emission, enhanced efficiency, and higher peak power than their undoped counterpart. Therefore, the active lasing ion type and concentration must be carefully optimized to maximize these benefits without the potential loss of thermal conductivity.

Every active lasing ion offers distinct advantages to laser technology and various applications, including specific spectral properties, energy levels, and lifetimes that make them suitable for various purposes. However, this thesis will concentrate on why the Yb^{3+} ion was chosen as a dopant in these materials (due to its unique characteristics) and relevance to the YAG and lutetia crystals. First, we will describe the relevance of the Yb^{3+} electronic structure and how it contributes to the thermal properties of its host crystal. Yb^{3+} has a simple two-level electronic structure (Figure 1.2), with one excited-state $^2F_{5/2}$ and a ground-state $^2F_{7/2}$. In principle, this would result in no gain and, consequently, no lasing capabilities since it operates as a two-level system. However, the degeneracy of the spin-orbit coupling splits the energy levels into sublevels (also named manifolds) through interactions of the local

environment with the host material via the Stark effect [11]. Given that Yb^{3+} has half-integer spin, the $^2F_{5/2}$ and $^2F_{7/2}$ energy levels form Kramer's doublets, leading to a degeneracy of $(2J + 1)/2$, where J is the total angular momentum quantum number [12]. Consequently, the $^2F_{5/2}$ and $^2F_{7/2}$ levels are divided into 3 and 4 sublevels, respectively, resulting in a total of $3 \times 4 = 12$ possible transitions as shown in Figure 1.2. This means that pumping and amplification involve transitions between the ground-state and excited-state sublevels, a process known as in-band pumping. This effect, resulting from closely spaced transitions, implies that the quantum defect remains consistently small in Yb^{3+}, enabling a high quantum efficiency of the laser transition. This property has the potential to facilitate high-power efficiencies and reduce thermal effects, which is one of the reasons why the Yb^{3+} ion is a desirable choice. Furthermore, what's particularly exciting is that Yb^{3+}-doped lutetia demonstrates nearly constant thermal conductivity even at elevated doping concentrations, thanks to the minimal ionic radius mismatch ($M_{Yb} \sim 173.04$ u, $M_{Lu} \sim 174.967$ u), potentially allowing for more lasing power without thermal issues (Figure 1.3) [10, 13].

The fiber core materials of YAG or lutetia, doped with Yb^{3+}, will also incorporate a cladding with its own distinct optical, thermal, and mechanical properties. As mentioned earlier, a cladding is a coating for the fiber core, comprising a material with a lower refractive index in contact with a core material with a higher refractive index. In this context, the core will be composed of either Yb^{3+}-doped-YAG or -lutetia, and the cladding will consist of undoped-YAG or -lutetia, respectively. YAG and lutetia have lower refractive indices than their Yb^{3+}-doped counterparts [13, 15]. The lower refractive index cladding effectively confines the light to the core through the principle of total internal reflection. This helps increase the laser gain through stimulated emission, where photons with matching energy levels interact with excited

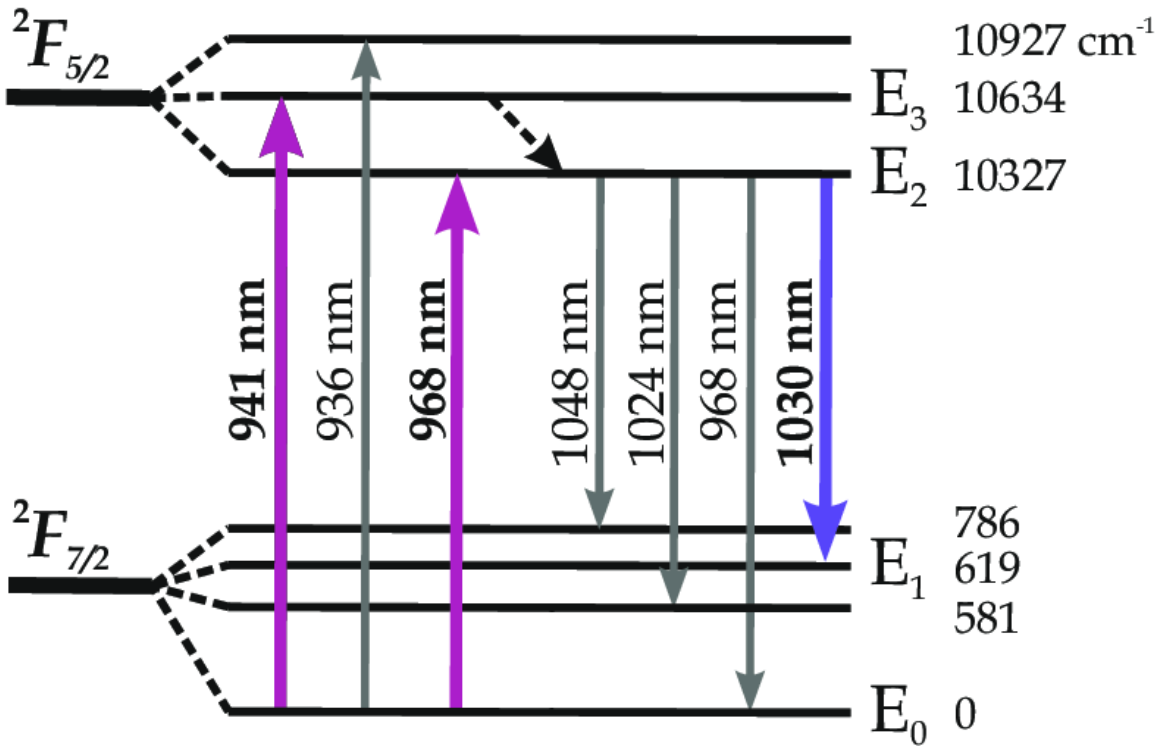

Figure 1.2: Energy level diagram of Yb^{3+} in YAG for various pumping modes. The dashed line between E_3 and E_2 represents a part of a quntum defect. Adapted from Ref [14].

atoms to produce additional coherent photons, thereby amplifying the laser beam's intensity. Thermally, the selection of cladding material is of paramount importance. Undoped -YAG and -lutetia exhibit slightly higher thermal conductivity as reported in previous studies [10, 13], causing the cladding to function as a heat sink. This is a crucial aspect as it efficiently dissipates heat from the core. Historically, claddings have commonly utilized polymers or silica glass, leading to the undesirable effect of trapping heat. Heat accumulation in the core material along the beam axis results in transverse refractive index gradients, resulting in thermal lensing. Additionally, this thermal stress can induce mechanical stress, potentially degrading the core-cladding interface and the core material. Hence, the selection of core-cladding materials and

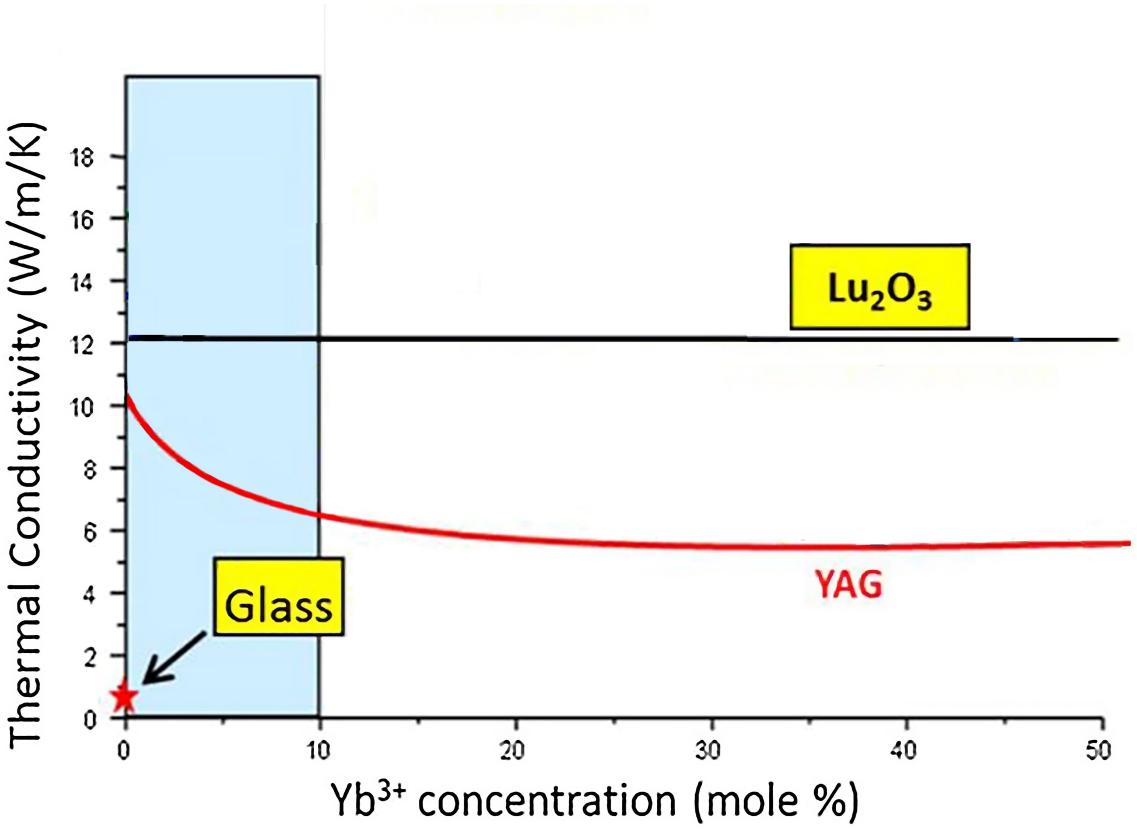

Figure 1.3: Thermal conductivity of YAG and lutetia as a function of Yb^{3+} doping concentration. Adapted from Ref [13].

meticulous fabrication processes are of utmost importance for ensuring effective thermal management and mechanical integrity of high-quality optical fibers capable of high-power operation. This thesis, therefore, focused on the development and implementation of optical fiber bend tests and the refinement of thermal conductivity measurement techniques on reference materials to ensure accurate measurements of YAG and lutetia optical fibers.

To assess the mechanical properties of optical fibers, we discuss a 2, 3, and 4-point bend test to determine the most suitable method for measuring the fiber's Young's modulus, which quantifies stiffness by evaluating the fiber's response to stress (force per unit area) and strain (proportional deformation). We also developed a

rudimentary bending model and instrumentation for the four-point bending test to elucidate the mechanical effects of cladding. This test offers numerous advantages, particularly for brittle fibers, as detailed in subsequent sections. Moreover, this system is still capable of testing the elastic regions of flexible optical fibers.

To examine the thermal conductivity of core-clad fibers, we employ the parallel thermal conductance technique [16]. This method enables precise thermal conductivity measurements for small, needle-like samples. The objective is to characterize the thermal conductivity of optical fibers, both with and without cladding, in order to gain insights into the properties of the core-cladding interface. Additionally, we discuss and test the potential use of the optothermal Raman technique (using graphene as an example), explaining how it can be applied to measure thermal conductivity by analyzing the interaction of light with the thermal properties of materials. Lastly, we explore the scalability of this technique to provide a more comprehensive description of the thermal conductivity of clad optical fiber systems.

Chapter 2

Young's Modulus Measurement of Mechanical Stress Due to Fiber Cladding

Variations of bend tests for optical fiber samples include the two-, three-, and four-point bend tests. These tests vary regarding the number of contact points and the location and manner in which an external force is applied to the sample. However, each test is designed to measure a given material's flexural strength and deformation behavior. Each test has its advantages and is best suited for different materials.

The two-point bend test was first described by Murgatroyd *et al.* [17] and improved upon by Matthewson *et al.*[18] by using a more detailed mathematical model and measurement system. This test is characterized by its two-contact point nature and is particularly well-suited for examining the behavior of flexible optical fibers and ribbon-like samples. In the typical setup of a two-point bend test (Figure 2.1), a sample is supported at two points, often using faceplates. These supports establish a span in which the sample is subjected to a load applied at its midpoint. As a

result, the sample experiences tensile stresses on one side and compressive stresses across the central axis, generating a bending moment. As depicted in Figure 2.1, the red trace of the bending moment distribution reaches its maximum at the midpoint, where the most significant internal shear forces occur. Meanwhile, the green trace of the shear force distribution exhibits a sign change based on the direction of the bending moment. While the two-point bend test configuration is valuable for assessing the bending behavior of optical fibers, some cladded optical fibers may not be well-suited for this testing method due to their inherent brittleness. Cladding can add a layer of fragility to the optical fiber, making it susceptible to fractures under the concentrated stresses generated in the two-point bend test. In such cases, alternative testing methods, such as the three- or four-point bend tests, may be more appropriate. These configurations distribute the bending stresses more evenly and can better accommodate the brittleness of cladded optical fibers, reducing the risk of sample failure during testing. However, due to their high flexibility, the intention for future work is to develop a two-point bend test for future work involving uncladded fibers.

In the three-point bend test (Figure 2.2), the sample is supported at two points, and a load is applied at the center. The additional support beneath the sample is crucial in evenly distributing the applied load, reducing localized stress concentrations. As a result of this load, the three-point bend test is characterized by a singular point where the bending moment reaches its maximum. The shear force is distributed across the sample support, with sign change at the center of the sample determined by the bending moment. This test configuration is particularly well-suited for assessing the mechanical properties of more rigid beams, primarily due to the effective distribution of shear forces and bending stresses. Although beneficial for assessing the mechanical properties of rigid materials, the distribution of shear

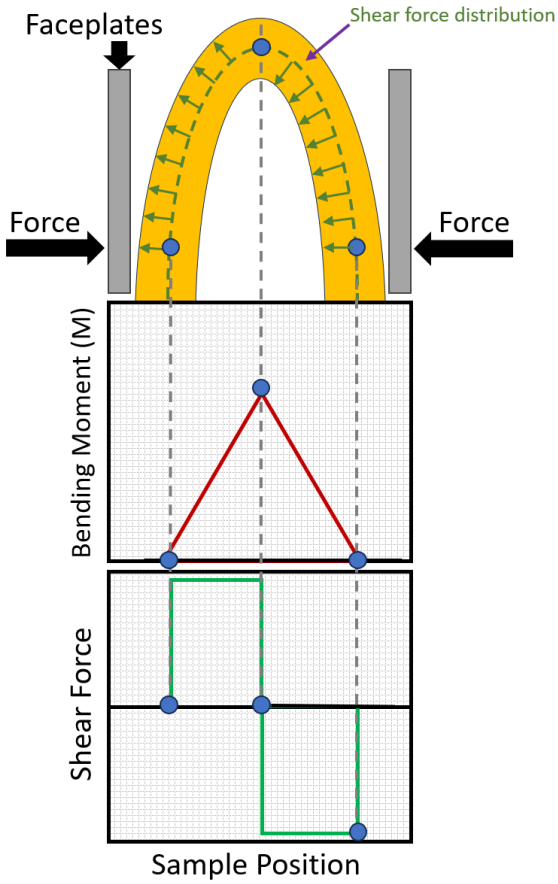

Figure 2.1: Two-point bend test diagram with bending moment and shear force distribution across sample position.

forces across the entire sample can pose a risk to cladded optical fibers, as it may subject the fragile sample to excessive stress. In such cases, a more suitable alternative may be the four-point bend test, which provides precise control over the location and magnitude of the applied force.

For cladded optical fibers made from materials like YAG and Lu_2O_3, the four-point bend test (Figure 2.3) is the preferred testing method. This testing configuration is chosen to mitigate the risk of damaging these fragile fibers during testing. The four-point bend test is a variation of the three-point bend test incorporating a fourth anvil, which applies a load on a specific fiber portion. In the four-point bend test, the

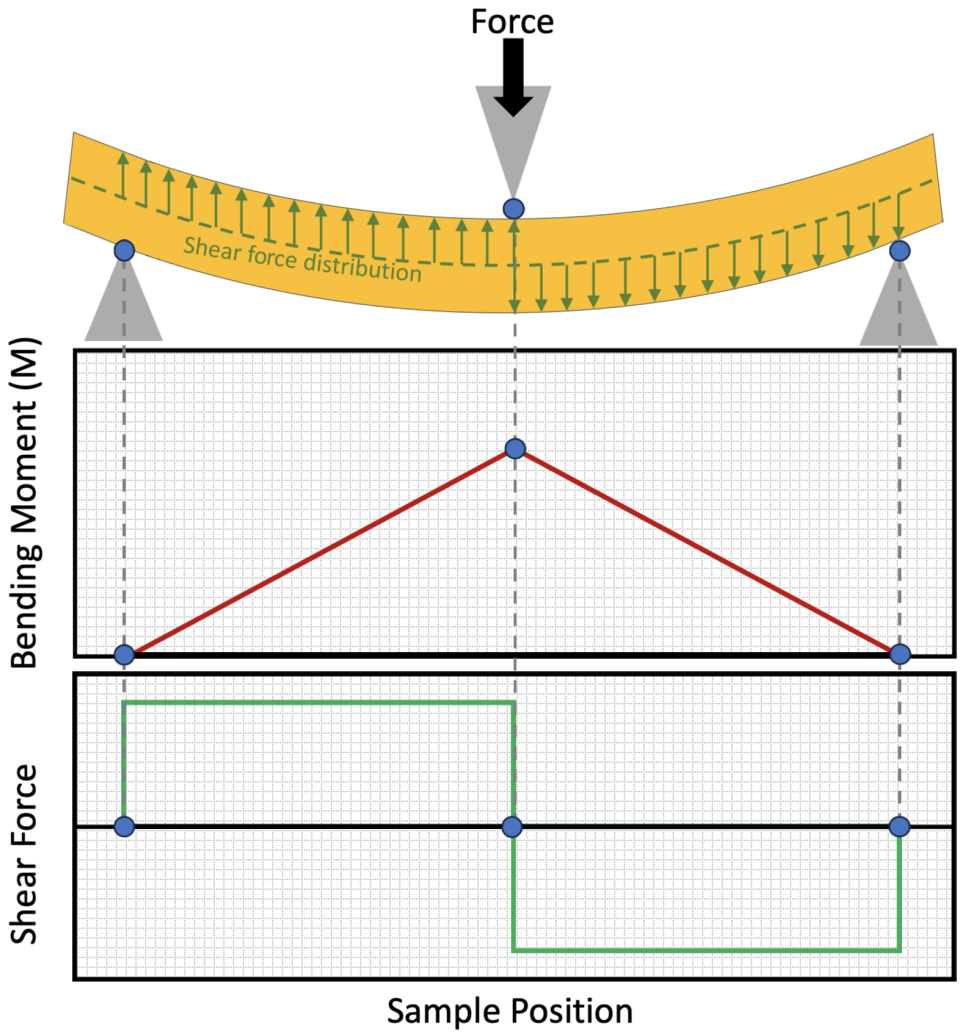

Figure 2.2: Three-point bend test diagram with bending moment and shear force distribution across sample position.

maximum stress occurs between two loading points and the supporting anvils rather than being directly under the central load, as seen in the three-point bend test. This is shown in Figure 2.5, where the green trace is non-zero only between the load and support anvils. This design minimizes shear forces between the two loading anvils. This test configuration ensures a constant bending moment distribution between the loading anvils along the sample. Consequently, it reduces the risk of sample damage, which facilitates the assessment's accuracy since the force's magnitude is distributed

across the sample position rather than having a singular maximum, as observed in the two-point and three-point bend tests.

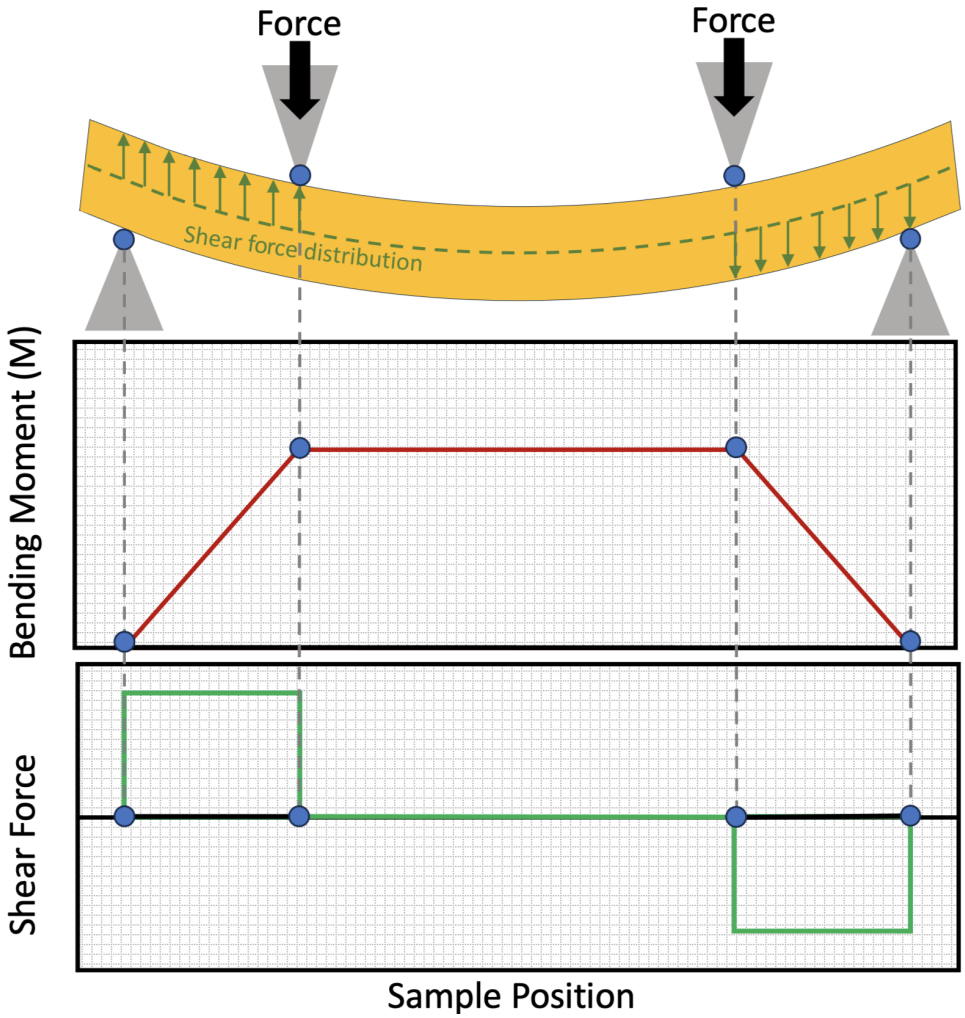

Figure 2.3: Four-point bend test diagram with bending moment and shear force distribution across sample position.

2.1 Mathematical Model for the Four-point Bend Test

The four-point fiber bend test setup, as depicted in Figure 2.4, is the foundation for our analysis. Before outlining the method, it is essential to mention some assumptions for completeness. 1) The beam is made of a homogeneous material with consistent and evenly distributed material properties. 2) The beam used in the test is straight and has a constant cross-sectional shape throughout its length. 3) Young's Modulus of Elasticity (E) value is the same in tension and compression. 4) The beam is subjected to pure bending (i.e., no external shear stresses). 5) The plane of symmetry of the beam aligns with the direction of the resultant loads applied to it, which ensures that the load distribution is even and predictable. 6) The cross-sectional shape of the beam is assumed to remain the same before and after bending, simplifying the analysis and allowing for a straightforward calculation of bending stress and deformation.

These assumptions are crucial in idealizing the behavior of the beam under bending conditions and simplifying the mathematical analysis of its response to applied loads. In practical applications, real materials and beams may differ from these assumptions, but these simplifications are often valuable for initial design and analysis. Our analysis will treat the sample as a solid cylinder with a uniform radius of r_0. Furthermore, we will assume that the sample is symmetrically positioned across the support span and that the load is applied symmetrically - a fundamental assumption because further analysis would be required in the case of asymmetry, as outlined in Ref. [19]. We aim to derive a few key parameters: the maximum bend strength σ and Young's modulus, denoted as E. We will start by using the bending equation for beams.

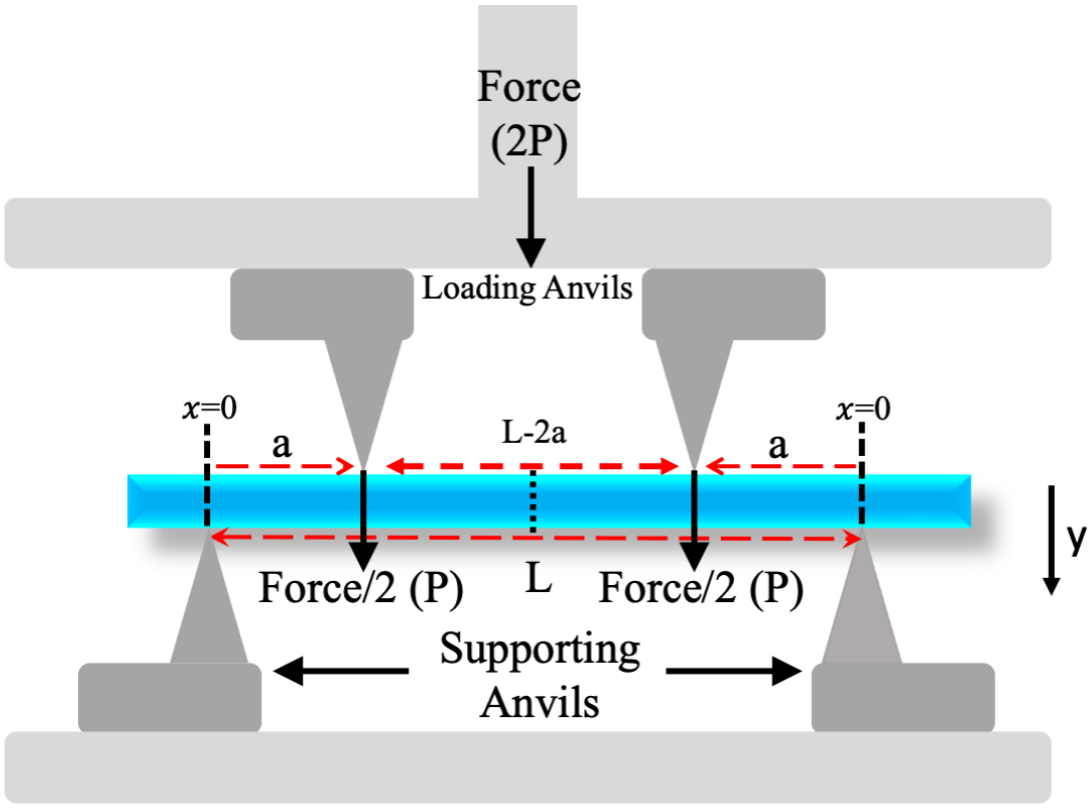

Figure 2.4: Four-point bend test setup

$$\sigma = \frac{My}{J} \tag{2.1}$$

Here, M represents the bending moment, y signifies the distance to the neutral axis, and J denotes the polar moment of inertia. The moment, M, is calculated by force, P, at a distance x from the midpoint of half of the sample (i.e., halfway between a). Next, we will calculate the bending moment that refers to the reaction induced in a structural element when an external force or moment is applied to the element, resulting in the element bending.

$$M = \sum_{n=1}^{2} P_n \cdot x = -P_{\text{left load}} x_{\text{midpoint to left loading anvil}} + P_{\text{left support}} x_{\text{midpoint to left support}}$$

$$M = -\frac{P}{2}(x - a) + \frac{P}{2}x = \frac{Pa}{2} \tag{2.2}$$

The distance from the neutral axis to the convex surface of the cylinder, y, is

$$y = r_0 \tag{2.3}$$

The polar moment of inertia is a measure of a beam's resistance to being distorted by torsion and is determined by its shape. The object's cross-sectional area solely influences this rigidity and does not depend on its material composition. The formula for the polar moment of inertia of a solid cylinder is as follows:

$$J_{\text{cylinder}} = \frac{\pi}{4} r_0^4 \tag{2.4}$$

Solving for σ in equation (2.1), the maximum bend strength of the solid cylindrical sample is

$$\sigma = 2\frac{Pa}{\pi r_0^3} \tag{2.5}$$

In the four-point bend test, the deflection, $y(x)$, of the entire beam is described by the following cubic equations, which describe how the natural axis curves due to its bending geometry [19].

$$y(x) = \frac{Px}{6EJ}(3aL - 3a^2 - x^2) \quad ; \quad 0 \leq x \leq a \tag{2.6}$$

$$y(x) = \frac{Pa}{6EJ}(3Lx - 3x^2 - a^2) \quad ; \quad a \leq x \leq L - a \tag{2.7}$$

Here, L represents the total length of the support span, a is the span between the supporting and loading anvils, and P is half of the force due to force analysis from one loading anvil position. For the measured deflection at the loading anvil position $x = a$, we can substitute $y(a)$ into the deflection conditions and obtain

$$y(a) = \frac{Pa}{6EJ}(3aL - 4a^2) \tag{2.8}$$

Rearranging for Young's Modulus, E

$$E = \frac{(3L - 4a)Ka^2}{6J} \tag{2.9}$$

where the substitution $K = P/y(a)$ is the bending stiffness. If we apply the equation 2.4 for a cylindrical system and align the beam such that $L = 4a$, we arrive at the relation

$$E = \frac{16}{3\pi}\frac{a^3}{r_0^4}K \tag{2.10}$$

Here, a and r_0 are predefined variables based on the optical fiber radius and the load and support span of the anvils. Therefore, the remaining variable is the bending stiffness K, the main parameter our system aims to measure. In the following section, we will delve into more detail on how to measure the bending stiffness.

2.2 Silica Optical Fiber as a Standard Reference Measurement

The four-point bender experimental setup was designed and built as part of my research projects (Figure 2.5). This setup includes an independent micrometer system that downwardly displaces the loading anvils equally onto the optical fiber, resulting in a measured deflection value denoted as $y_m(a)$. Upon contact, this records a mass reading on the scale, from which P can be easily calculated using the gravitational constant (9.81 m/s^2). Again, the values for the total length of the bottom support span (L), the difference in length between the support and loading anvils (a), and the polar moment of inertia (J) are predetermined. The bending stiffness K is the ratio of half of the force to the measured deflection $P/(y_m(a))$ as determined by the micrometer and scale.

To evaluate the accuracy of this system, a bare SiO_2 optical fiber with a diameter of 150 μm was utilized as a reference for calibration (see Figure 2.5). The total length of the fiber was measured using a Mitutoyo 293-761-30 Digital Micrometer and determined to be 59.50 mm. The sample was symmetrically positioned along the bottom support span with a total length of $L = 28.0$ mm, meaning each supporting anvil was placed at $L/2 = 14.0$ mm from the origin. Similarly, the top loading anvils were placed along the top of the load span, each at $L/4 = 7.0$ mm from the origin. This initial symmetry is essential based on the assumptions derived in Section 2.2. The bending stiffness (Figure 2.6) was determined to be $K \sim$3.9 N/m from the slope of the force versus deflection curve. Plugging these values into equation 2.9 yields $E \sim$72.3 GPa. However, the accepted E value for bare $SiO_2 \sim$72 GPa [20]. This suggests that the experimental error from our setup is $< 1\%$. The result has been successfully replicated; however, the precision of this measurement leaves much to be desired.

To enhance precision, we should consider employing more accurate instrumentation and optimization techniques. This may involve using a more sensitive scientific scale with higher precision, favored weighted averages, and more bandwidth for deflection measurements (scale is currently limited by its total mass load).

Additionally, implementing a laser alignment system and making other refinements to the experimental setup could further improve the precision of this measurement as equation 2.10 has a^3 dependence. In the context of applications to cladded optical fibers, it's essential to acknowledge that this method needs refinement due to the cladding and core modulus mismatch before accurately and precisely determining their mechanical material properties. However, this method serves as a useful baseline and proof of concept that can be further developed.

Figure 2.5: A four-point bender experimental setup that was designed and built at Clemson Nanomaterials Institute (CNI).

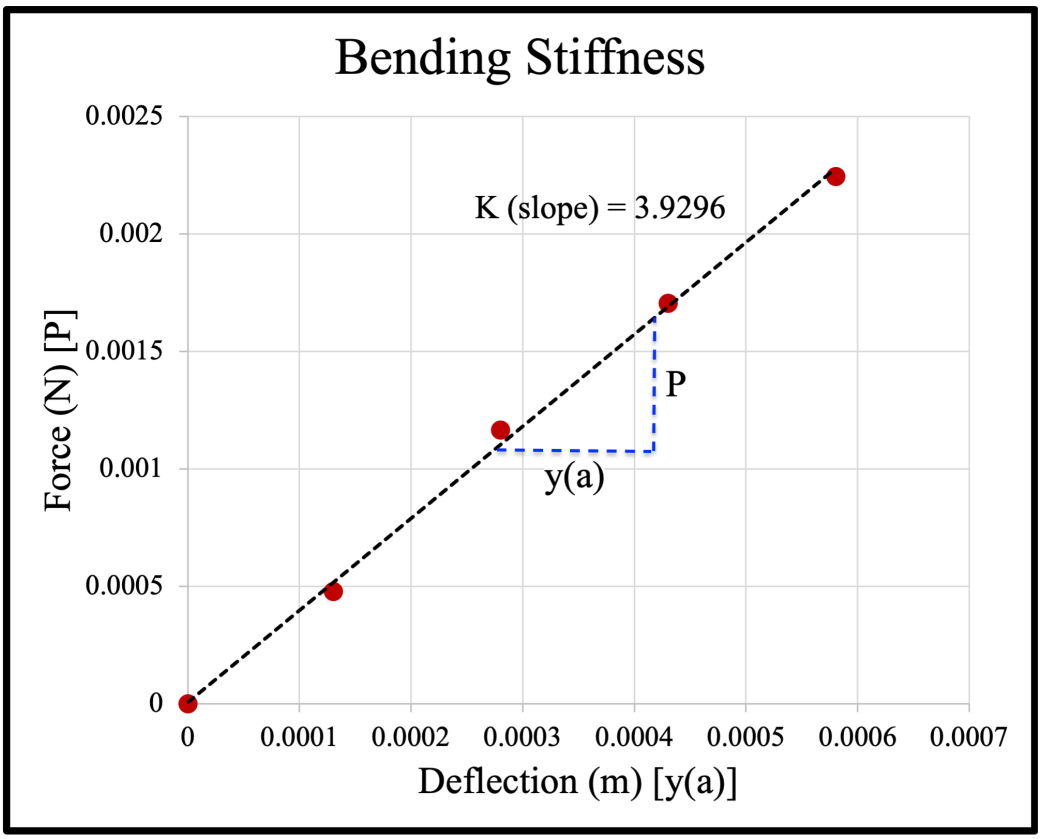

Figure 2.6: Bending stiffness graph for a bare 150 μm SiO_2 optical fiber. The slope describes the force required to displace the sample.

Chapter 3

The Parallel Thermal Conductance Technique

3.1 Overview

The parallel thermal conductance (PTC) technique is a steady-state method that Tritt and coworkers developed [16] to address the challenges of working with small diameter needle-like samples, typically less than 1 mm in at least two dimensions, which cannot accommodate a heater and thermocouple system, as required for conventional measurements. Indeed, transient techniques have been developed for small samples, such as the 3ω [21] or pulse technique [22], but can often require a substrate with extensive preparation and calibration, as in the case of 3ω technique. However, the PTC technique offers numerous advantages for small samples thanks to its ease of use and capacity to accurately characterize thermal conductance, which it achieves by minimizing radiation losses, heat conduction and convection. The term ''parallel'' originates from the configuration that facilitates heat flow through two distinct materials in parallel – namely, the sample and the supporting post composed of a thermally

insulating material. Figure 3.1 shows the electrical analog circuit diagram. In this configuration, a heater serves as a power source within a parallel circuit of thermal resistors. The total thermal resistance (R_{total}) of the analog circuit can be best described by the following equation:

$$\frac{1}{R_{total}} = \frac{1}{R_{sample}} + \frac{1}{R_{baseline}} \tag{3.1}$$

The total conductance (C_{total}) of the system is therefore

$$C_{total} = C_{sample} + C_{baseline} \tag{3.2}$$

Here, it is shown that to characterize a sample, a baseline of conductance in our thermal circuit must first be measured, which can be subtracted from a total conductance measurement to obtain our sample 's thermal conductance.

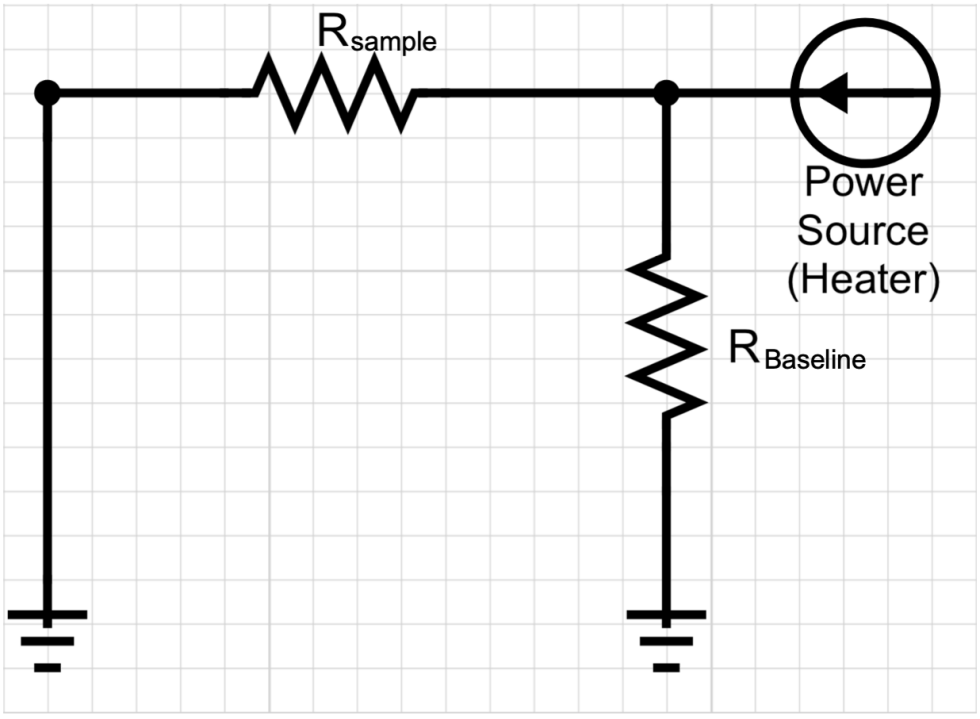

Figure 3.1: Electrical analog of the PTC system measurement.

The PTC system, which was non-operational when acquired by Clemson Nanomaterials Institute in 2022, is currently undergoing restoration to measure the thermal conductivity of optical fibers. The PTC technique can measure the thermal conductance of thin wire samples. For example, carbon fibers, with diameters ranging from 10 to 100 μm, have been documented in previous studies [16, 23]. This makes it well-suited for measuring the thermal conductivity of cladded optical fibers, which often have a diameter of 150 μm or smaller. Furthermore, it can measure the thermal conductivity of the core material and the core-clad optical fiber.

The PTC technique involves two measurements of thermal conductance. The first step is conducting a preliminary measurement of the sample holder. This measurement establishes a baseline for thermal losses associated with the specific sample stage. The second step involves mounting a sample and then conducting a second measurement of the thermal conductance of the entire system. The sample's thermal conductance is calculated by subtracting the baseline measurement from this second measurement. However, to calculate thermal conductivity, the cross-sectional and length elements of the sample need to be accounted for. By applying Fourier's law of heat diffusion at steady-state, we can relate thermal conductivity as follows,

$$\kappa = \frac{P}{\Delta T}\frac{L}{A} \tag{3.3}$$

Here, P represents the power passing through the sample, κ denotes the thermal conductivity of the material, A is the cross-sectional area, and L is the length of the sample, where the temperature difference, ΔT, is determined. Equation 3.3 indicates that a ''power sweep'' can be conducted by adjusting the applied power to the system while measuring the temperature gradient resulting from the response of the material's thermal properties. This is the core relationship that the PTC technique

seeks to measure and will be elaborated upon in subsequent sections.

3.2 The Sample Stage

The sample stage schematic is provided in Figure 3.2, while a photo depicting its real-life construction is given in Figure 3.3. The primary design objective of the PTC sample stage is to minimize the thermal conductance of its components in comparison to the sample's conductance. Ideally, the magnitude of the sample's thermal conductance should be at least one-tenth that of the sample stage (baseline) to ensure an adequate signal-to-noise ratio for good resolution [16, 24]. To achieve this, the sample stage is designed with a thin strip of commercially available PET inkjet transparent film sandwiched between a copper base and a copper support structure. One end of the copper support facilitates heat conduction through the sample and ensures its ability to reach and maintain a steady-state temperature condition. In addition, the inkjet transparent film is utilized on one end of the support to uphold the sample, heater, and thermocouple. This film isolates the copper base from any potential thermal effects from the heater and ensures that heat solely flows through the sample, avoiding any heat loss to the sample stage. This design minimizes heat loss to the sample stage, allowing one end of the sample to maintain ambient temperature and create a temperature gradient across the sample. The choice of film is based on its low electrical and thermal conductivity and structural stability. Moreover, it is flexible enough to accommodate contraction as the system cools.

Additionally, a 120 Ω strain gauge is used as a low-power heater and attached to the sample's end. This strain gauge generates heat by applying a small current to create resistive heating within its heating element, thus creating a controlled temperature gradient in the sample. A 1 mil Constantan-Chromega-Constantan (CCC)

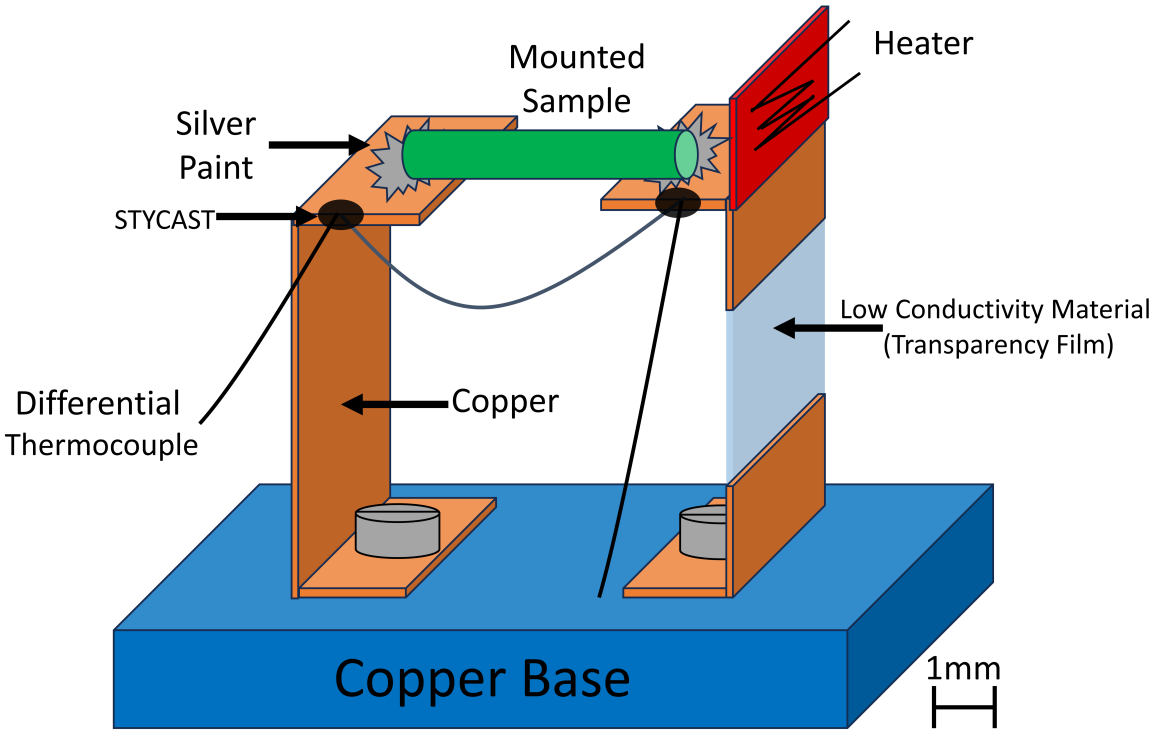

Figure 3.2: Schematic of the PTC sample stage depicted with a mounted sample.

type E differential thermocouple is utilized to measure this temperature gradient. This specific thermocouple type is selected for its responsiveness and ability to maintain performance at cryogenic temperatures without junction degradation. They are also sufficiently small to ensure negligible thermal conduction through the wires. The temperature difference across the sample is determined by measuring the Seebeck voltage between the two ends of the sample using a meticulously calibrated differential thermocouple. To support the junctions of the thermocouple, they are mounted on the copper supports using Stycast # 2850FT, Catalyst 9, a thermally conductive electrically-nonconductive epoxy encapsulant. It is essential to electrically isolate the thermocouple (to ensure the proper functioning of its junctions) but still be in thermal contact with the system. Once the sample stage is appropriately prepared, a baseline

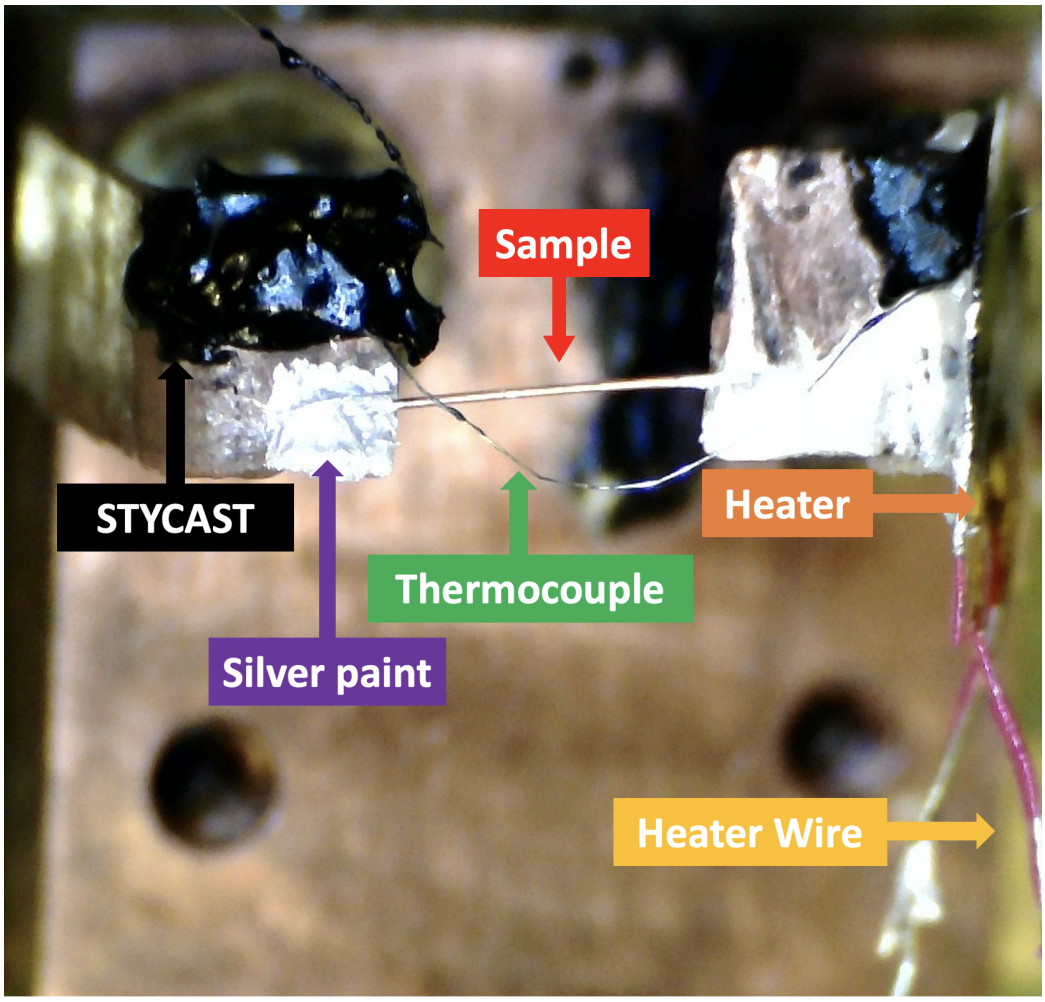

Figure 3.3: Photograph of the PTC sample stage with a mounted sample.

measurement is recorded. It's essential to emphasize that a baseline measurement should be taken before mounting each sample to ensure accuracy. This precaution is necessary because any potential damage or alterations to the sample holder could affect its thermal conductance. Once the baseline is characterized, a sample is attached to the stage using a minimal amount of silver paint (DuPont 4929N). This silver paint serves as cement to ensure the sample's stability and provides the same conductive benefits as previously mentioned about the copper support.

3.3 System Overview

The system setup is illustrated in Figure 3.4. First, the system is evacuated to at least 10^{-6} Torr pressure using a Leybold PT 151 Turbomolecular Pump. It is essential to use a high vacuum to minimize gas heat conduction and convection losses. Next, an ARS-2HW Helium Compressor and an ARS DE 202N Closed Cycle Cryocooler are employed to cool the system from room temperature to ∼20 K. Following the initialization, the PTC system is controlled by a LabVIEW program, which communicates with the instruments via a GPIB interface. A Lakeshore 340

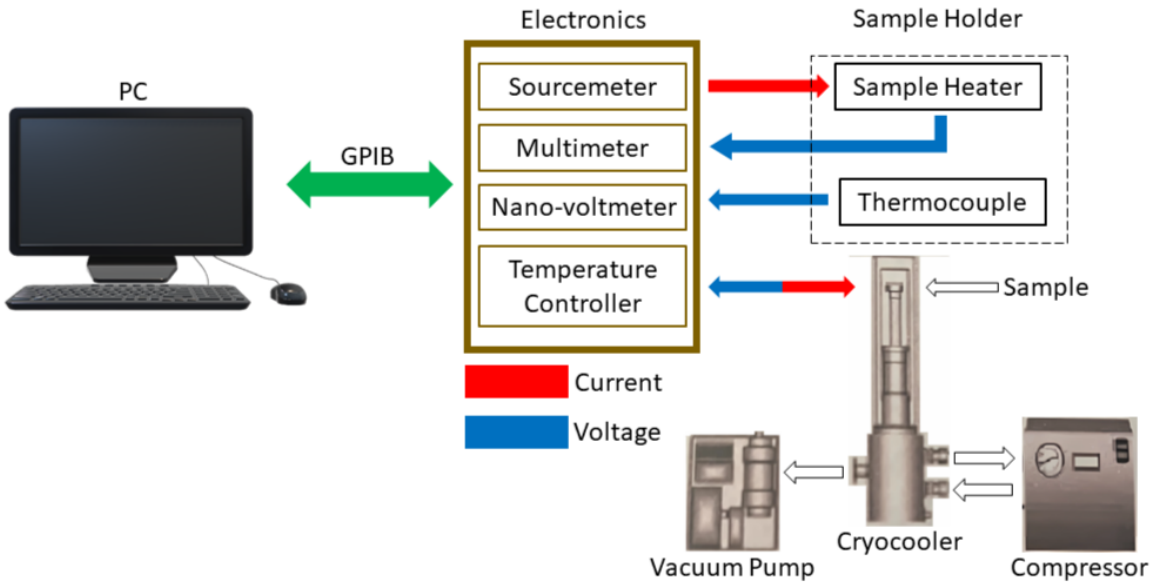

Figure 3.4: Schematic of the PTC system [24].

Temperature Controller is used to regulate the temperature of the sample base, assisting in maintaining thermal equilibrium within the sample holder. A Keithley 2400 Sourcemeter provides current to the strain gauge heater, while a Keithley 2001 Multimeter measures the voltage across the heater, determining the heater's power output.

A Keithley 182 Sensitive Digital Nano-voltmeter is used to measure the voltage across the differential thermocouple near the sample, essential for determining the temperature gradient. A Kurt J. Lesker Series 979 Atmosphere to Vacuum Transducer [25] monitors the pressure. This device combines a hot cathode sensor to measure pressure from 5×10^{-10} to 3×10^{-3} Torr and a MicroPirani sensor for pressure ranges between 1×10^{-3} Torr to atmospheric pressure. The hot cathode gauge measures the ultra-high vacuum pressures by regulating electron current from a heated filament, leading to gas ionization in the chamber. The ion count is proportional to gas molecule density and electron current.

3.4 System Operation

The PTC LabVIEW program was developed by Zawilski *et al.* [16] and is responsible for the remote control and regulation of the necessary data acquisition and calculations. The program panel can be seen in Figure 3.5. To operate the program successfully, the user must provide specific inputs, including the sample's cross-sectional area, the length between the two ends where the sample is attached, and the desired number of sampling points. Geometry inputs are crucial because we are measuring thermal conductance. However, our goal is to describe thermal conductivity, and any geometric considerations can be factored out to better characterize the intrinsic material properties.

The program handles all instrument configurations, and data acquisition proceeds via the flowchart depicted in Figure 3.6. Once the system is initialized, it commences at the lowest temperature specified by the user. Upon reaching the desired temperature, the system's parameters are held for 180 seconds to ensure a stable temperature within $\pm$ 25 mK. This holding period allows ample time for the sam-

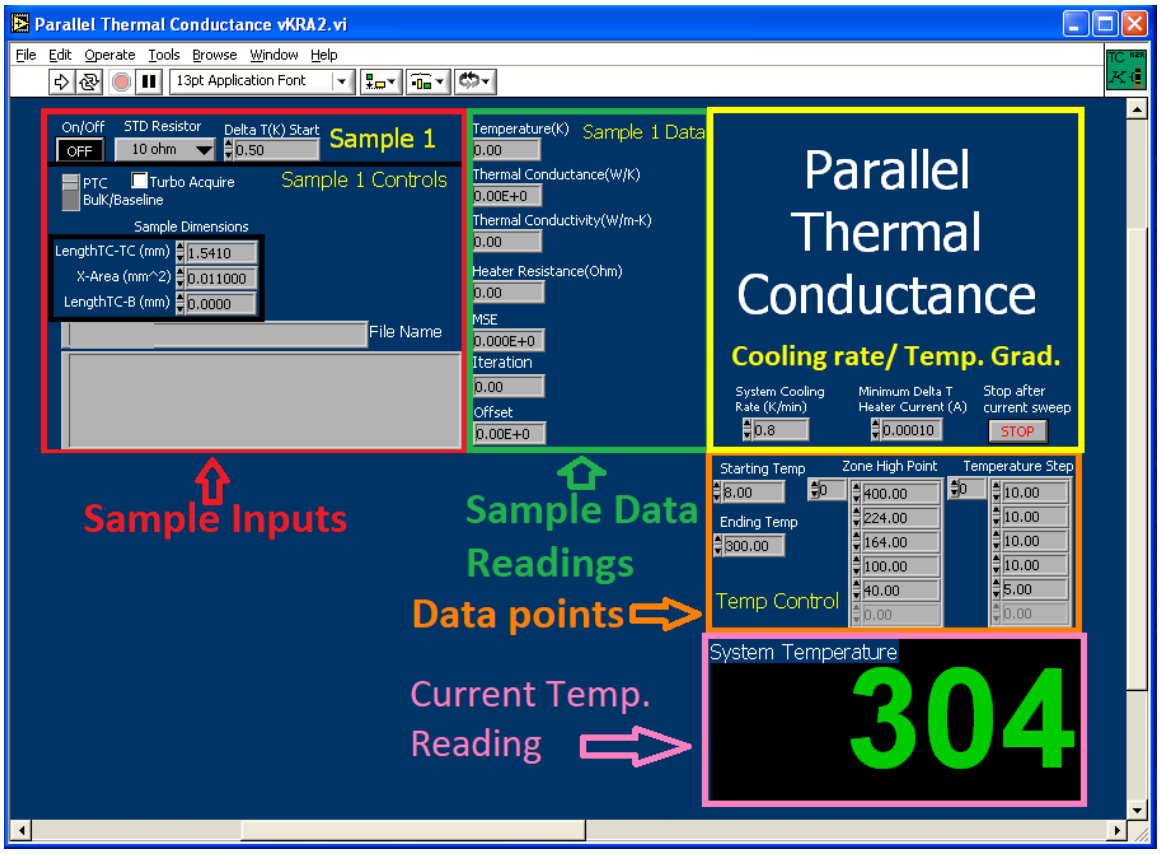

Figure 3.5: The PTC program control panel [16].

ple and surrounding environment to reach a steady-state condition. After this time, power is applied to the strain gauge to heat the sample and create a temperature gradient. Again, for the same reason, the system is held for 180 seconds for a stable temperature gradient. Once stable, the system advances to the data acquisition phase, which consists of performing a "power sweep" (P vs. ΔT), as mentioned in the previous section. To achieve this, varying amounts of small currents are applied to the strain gauge, resulting in different temperature gradients within the system until at least three measurement points are recorded, up to a predefined maximum power output. The sample temperature is determined by adding half of the temperature gradient values to the base temperature for each data point in a power sweep (Figure

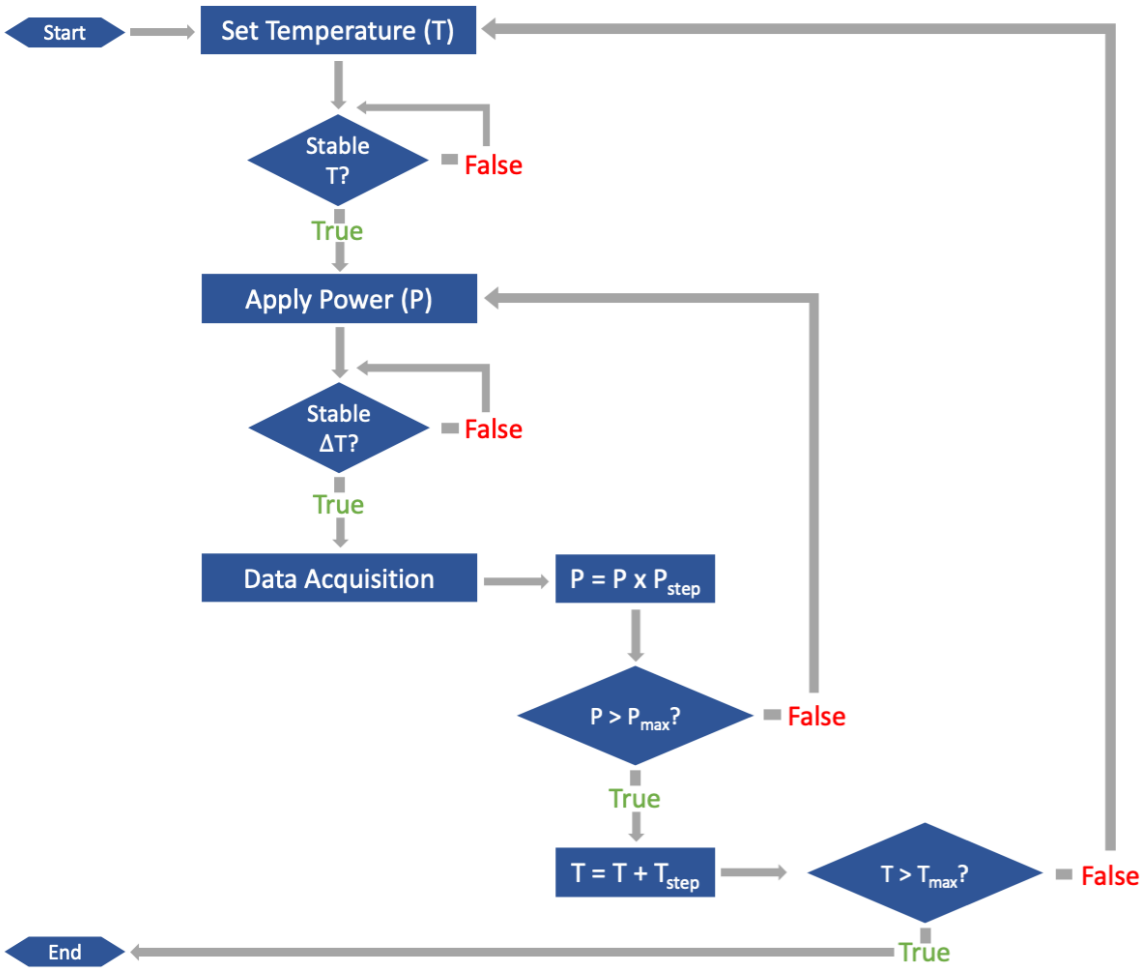

Figure 3.6: Flowchart for the measurements conducted by the PTC system [24].

3.7). This process is repeated for different sample temperature values, with the temperature incrementally raised while acquiring data at predefined intervals until the final temperature is reached. The program's next step involves fitting a straight line to the recorded data obtained from each power sweep. This fitting process ensures that at least three data points are used for better accuracy than a single data point or even two. By fitting a straight line to the data, the program determines the thermal conductance of the sample at the specific temperature under consideration. Following this, the baseline at that temperature is subtracted, and the sample dimensions are considered to calculate the thermal conductivity.

3.4.1 Development of the PTC System and a Standard Reference Measurement

The PTC system required significant work. For example, its sample stage components were either damaged, parts were misappropriated, or completely disassembled. The sample stage needed to be reassembled to specification and constructed for optical fiber measurements to resolve these issues. Furthermore, the entire system needed to be reassembled, and some components were rewired to restore functionality.

First, the supports for the sample stage were constructed. Most importantly, differential thermocouples were created because no 1-mil CCC differential thermocouples were commercially available. This was achieved by welding the proper junctions together using a thermocouple welding setup (see Figure 3.8). In this setup, a power supply charged the capacitors in series to build up a predetermined voltage potential. For 1-mil CCC, the ideal voltage range was around 2-4 V. This potential was discharged by completing a circuit with a foot-operated switch and tapping a knife edge on an intersection of the thermocouple wires. This process quickly heated the

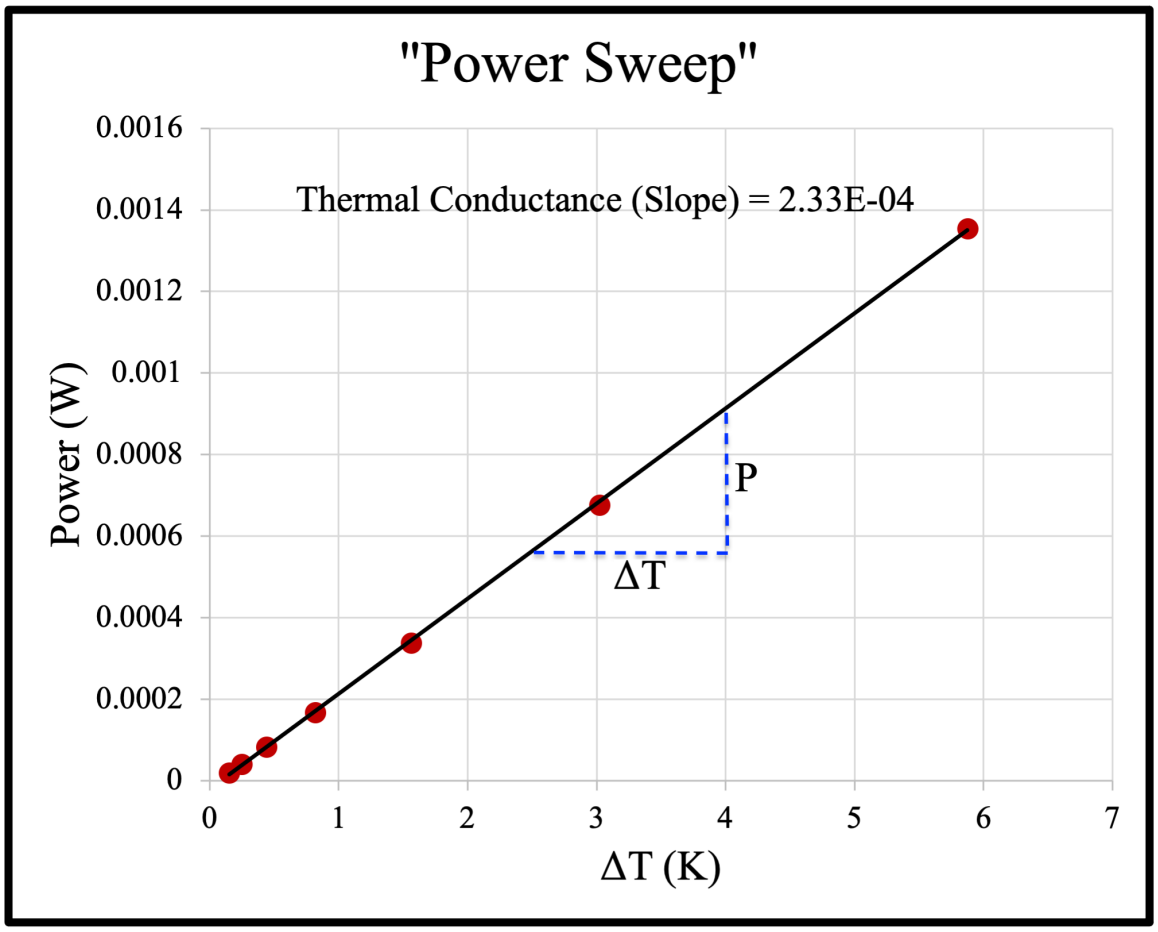

Figure 3.7: Example of a power sweep performed for a baseline measurement, where the slope represents thermal conductance.

intersection of the wires through resistive heating, resulting in a weld at the junction. While preparing the thermocouple is straightforward in theory, the small size of the components made this a challenging task. Once the differential thermocouples were created, they were mounted as described in previous sections. Subsequently, the strain gauge was also soldered and mounted on the system.

To ensure the system's proper functioning, we identified and addressed wiring shorts. This straightforward process involved establishing proper contacts to complete the necessary circuits. After addressing the wiring issues, the system was tested by

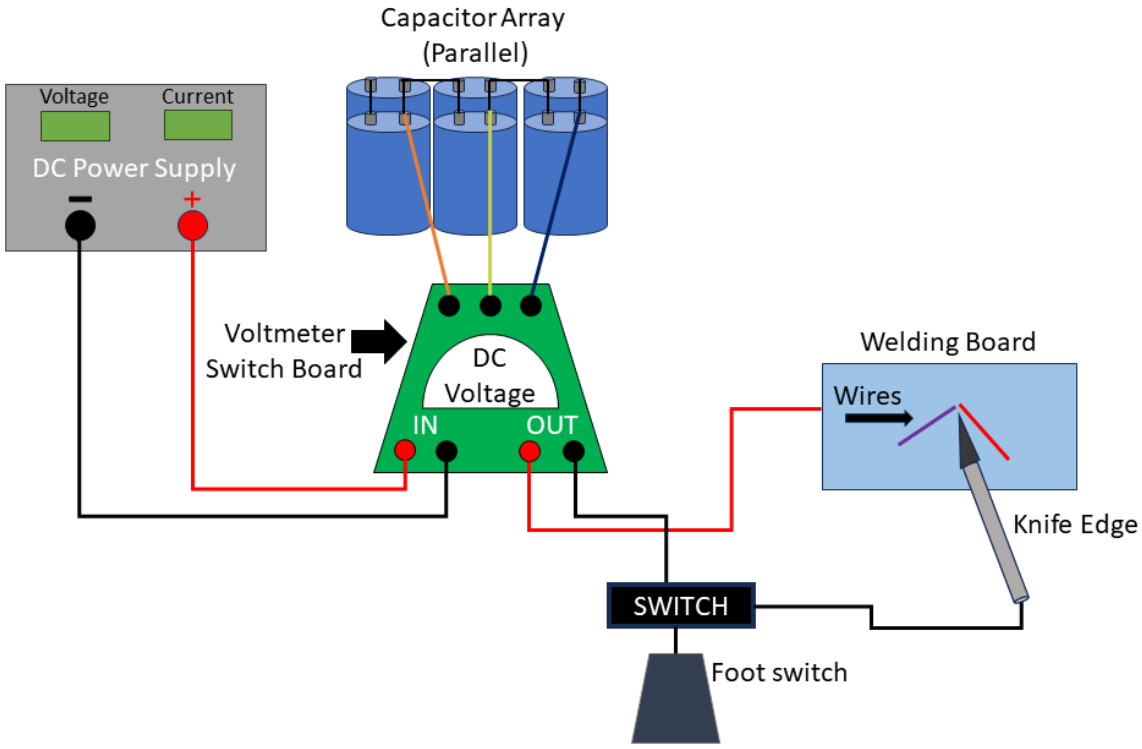

Figure 3.8: Thermocouple welding setup.

members of Clemson Nanomaterials Institute (CNI) first without a sample to establish a baseline and later with a standard reference sample of phosphor bronze (see Figure 3.9b), which is a copper-based alloy with tin and phosphor present. The equation 3.3 can be applied where the measured cross-sectional area $A = 0.016$ mm^2 and a length $L = 3.60$ mm were used to calculate the thermal conductivity of the standard reference sample of phosphor bronze. The calculated κ at various temperatures is given in Figure 3.9a. Here, the CNI labeled data is the most up-to-date data recorded by the lab members restoring the PTC's functionality. The Tritt Group/S. Bhattacharya data is former data from the previous Clemson University group that developed the PTC technique. The referenced data is shown for comparison, where Ref. [26] shows a trace that is characteristic of radiation losses above $\sim$ 150 K. Ref. [27] is historical

data from 1956 that was reported to values lower than 100 K. Here Figure 3.9 shows a divergence of thermal conductivity values which are possibly explained by heat sinking and radiation losses associated with each system's setup.

To gain insight into the thermal transport of a standard reference sample of phosphor bronze, the total measured thermal conductivity (κ) from the PTC can be broken down into electronic (κ_E) and lattice (κ_L) components.

$$\kappa = \kappa_E + \kappa_L \tag{3.4}$$

For pure metals $\kappa_E >> \kappa_L$, therefore, we can apply the Wiedemann-Franz law to calculate the electronic contribution.

$$\kappa_E = \frac{L_0 T}{\rho} \tag{3.5}$$

Here, T is the temperature, ρ is the electrical resistivity, and L_0 is the Lorenz constant (2.44×10^{-8} WΩ/K^2). To calculate κ_E, the temperature-dependent data of ρ from Ref. [26] was used. Due to phosphor bronze's high electrical conductivity, it is expected that κ_E contributes to a higher percentage of the total thermal conductivity. Figure 3.10 illustrates this, where κ_E dominates at temperatures above $\sim$40 K. However, at temperatures below $\sim$50 K, the lattice contribution plays a greater role in thermal conductivity. Generally, Fourier's law of heat conduction applies to 3D materials to describe diffusive heat transport; however, it is well known that this law breaks down in the ballistic and hydrodynamic regimes in 3D materials at extremely low temperatures $\sim$0.5-1 K, much lower than the temperature range measured using the PTC system [32]. Figure 3.11 shows an Umklapp peak in the lattice thermal conductivity around 50 K [33, 34]. Here, the peak height is suppressed due to mass fluctuations from the other non-copper elements [35]. Furthermore, the rise of the

peak around 150 K is possibly attributed to radiation losses.

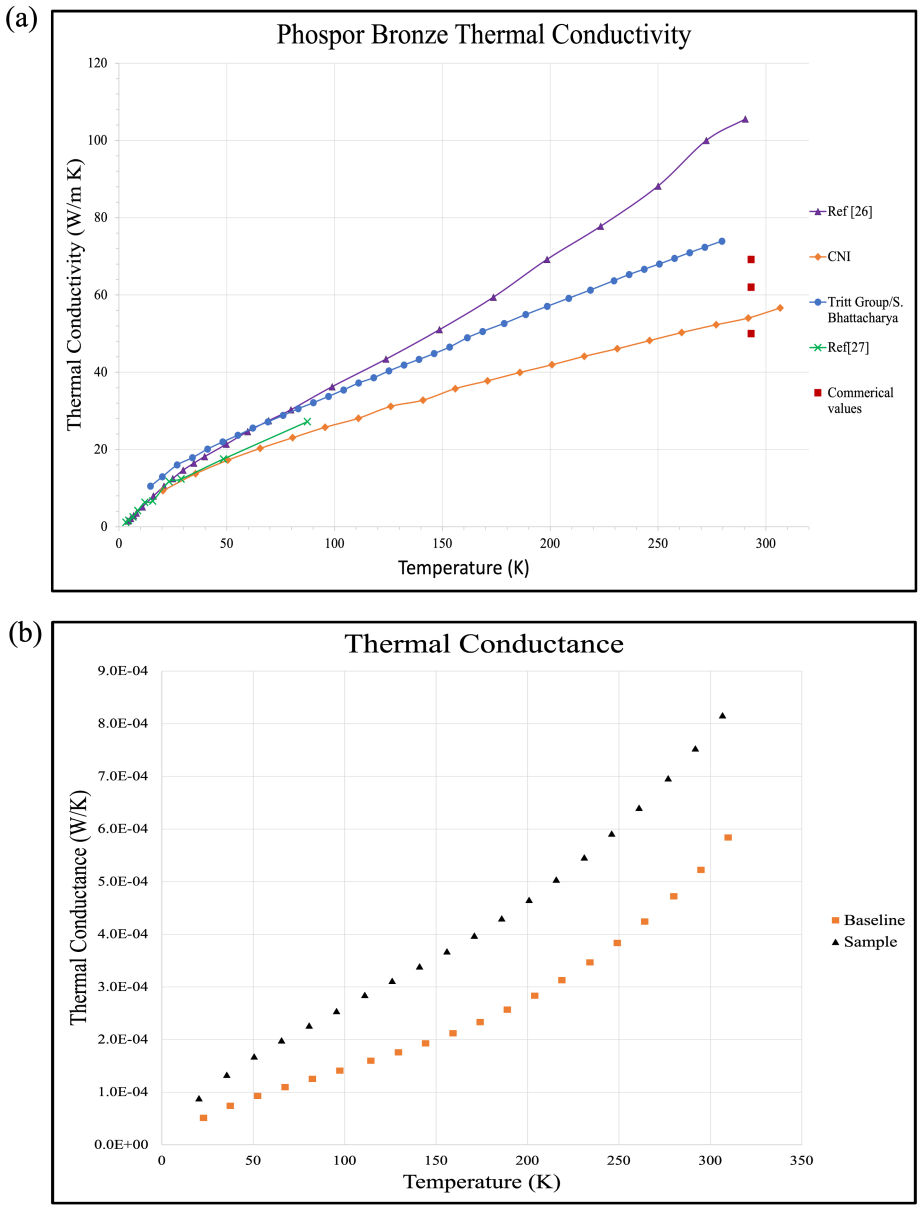

Figure 3.9: (a) Thermal conductivity for a reference sample of phosphor bronze. Each data point represents the thermal conductivity at a given ambient temperature value. The most up-to-date data, as reported in this thesis, is denoted by the orange $\diamond$ rhombus symbol. The Tritt Group/S. Bhattacharya blue circle symbol $\circ$ is old data from the Clemson University lab that helped develop the PTC technique [16]. The purple triangle $\triangle$ symbol data from Ref. [26]. The green $\times$ symbol is historical data from Ref. [27]. The red square $\square$ indicates commercially available phosphor bronze values from Refs. [28–31]. (b) Thermal conductance for the sample stage as a baseline and the phosphor bronze sample thermal conductance from the CNI data.

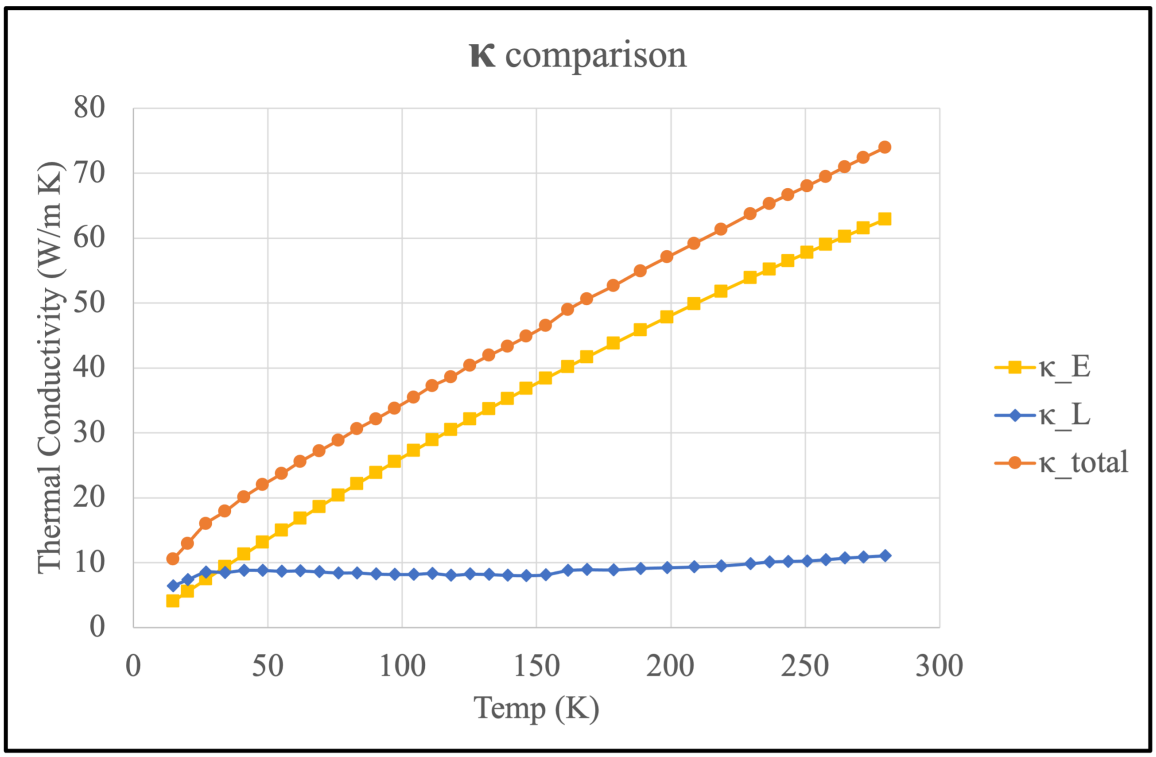

Figure 3.10: The total thermal conductivity κ measured by the PTC system where κ_E shows the electronic contribution calculated by the Wiedemann-Franz Law. The lattice contribution κ_L is then determined by subtracting κ_E from κ.

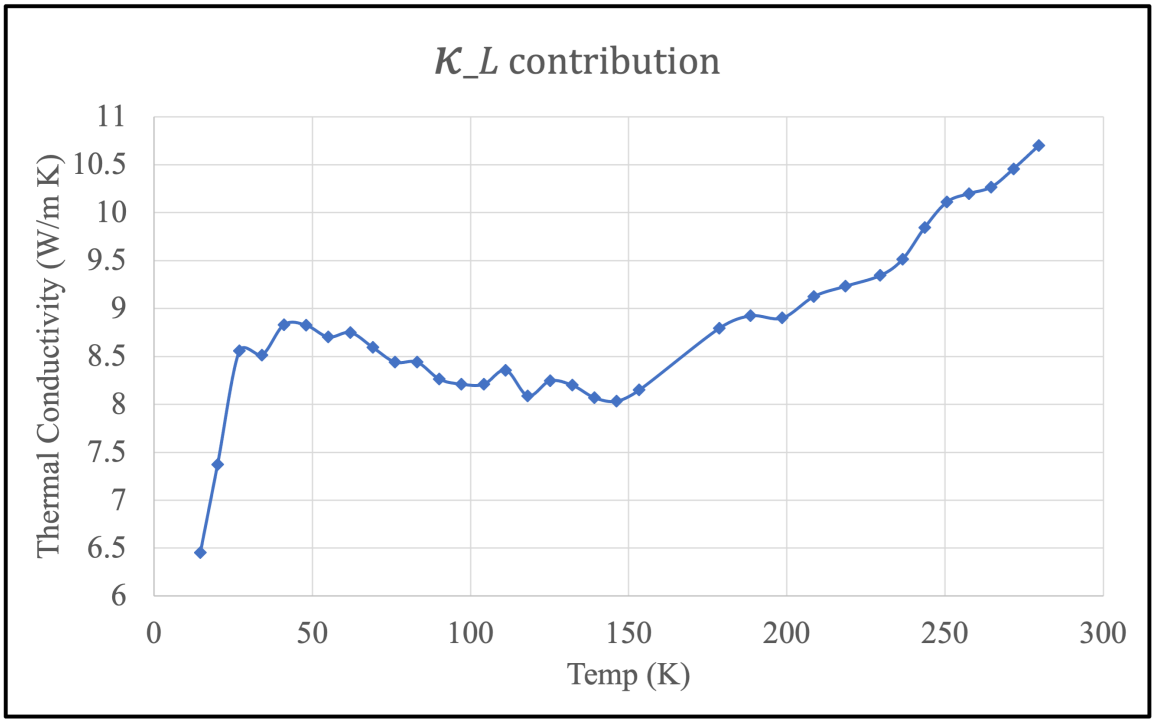

Figure 3.11: Lattice thermal conductivity (κ_L) contribution in phosphor bronze.

Chapter 4

Future Research: Optothermal Raman Method

An alternative approach to determining the thermal conductivity of optical fibers involves ''optothermal'' techniques. This term combines ''opto'' and ''thermal'' to describe phenomena that entail the interaction of light (optical) to generate heat (thermal). Specifically, optothermal spectroscopy refers to a technique that uses laser light to locally generate heat in a sample and measure the resulting thermal effects through changes in the absorption or emission of light. In particular, the optothermal Raman technique enables the study of individual vibrational modes. This approach allows for examining the contributions to thermal conductivity from various vibrational modes, with each mode potentially exhibiting significantly different thermal conductivity, particularly in the case of anisotropic materials. In the context of cladded optical fibers, this technique can potentially be employed to analyze the interfacial thermal conductance between the core and cladding, allowing for the identification of radial heat flow. Additionally, it can serve as a valuable point for comparing the thermal conductivity with the PTC technique. In the following sections, we will derive the

two-dimensional case of the OTR technique to provide a baseline for understanding the thermal conductivity of thin-film systems with a preliminary standard reference measurement to verify our technique and analysis. Subsequently, we will extend this knowledge to gain insights into higher-dimensional systems like optical fibers and explore how the OTR technique can be applied in larger-scale systems.

4.1 Description of the General Optothermal Raman Technique

The optothermal Raman (OTR) technique is a steady-state no-contact technique introduced by Balandin *et al.* [36] for measuring the thermal conductivity of low-dimensional materials [37–43]. The initial setup is shown in Figure 4.1, where a suspended material on a substrate is under investigation. The OTR method adopts a two-step process to measure thermal conductivity. First, Raman peak shifts are recorded as a function of absorbed laser power (χ_P). Here, laser light is used to heat the sample locally, approximated by a Gaussian distribution where the induced temperature rise causes bond softening, resulting in Raman peak frequency shifts. The total power, P_D, is measured by a detector and is equal to the sum of total powers absorbed by the suspended material (P_α) and the substrate (P_S), $P_D = P_\alpha + P_S$. The power absorbed by the material is then approximated such that $P_\alpha = I_0 A(1 - \exp(-\alpha t)) \approx \alpha t I_0 A$, where A is the illuminated area, I_0 is the laser intensity on the surface, α is the absorption coefficient of the material and t is the thickness of the material. The second measurement is to record the temperature-dependent Raman peak frequency shifts (χ_T). To do this, the suspended material is placed in a hot/cold cell where the temperature is controlled externally, and Raman

wavenumber shifts are recorded as a function of temperature.

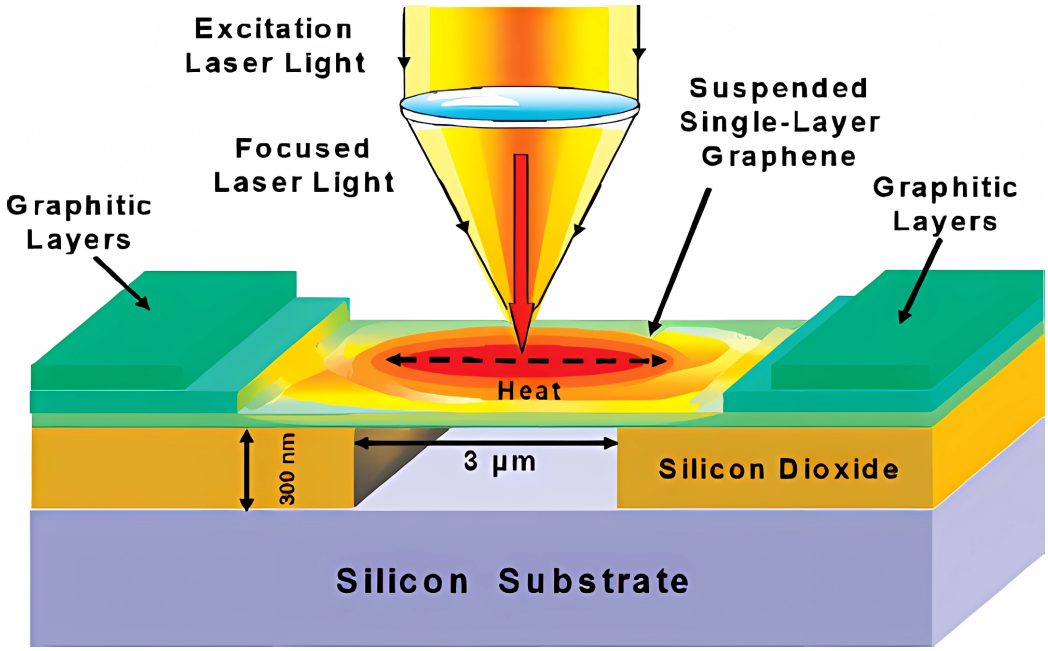

Figure 4.1: Schematic of original OTR technique. Graphene is suspended over a 3μm rectangular trench where a laser is utilized to locally heat the sample [36].

Thermal conductivity is derived using Fourier's law,

$$\frac{\partial Q}{\partial t} = -\kappa \oint \nabla T \cdot dS \tag{4.1}$$

Here Q is the total heat transferred over a time t, and T is the absolute temperature of an infinitesimal element dS. The steady-state condition allows κ to be defined and expressed as

$$\kappa = \frac{\chi_T}{\chi_P} \frac{L}{2tW} \tag{4.2}$$

where L denotes the distance from the center of the sample to the substrate edge, and W is the width. However, this model is limited due to the description of a cylindrical heat distribution over a square domain with unaccounted substrate effects

[36, 44].

To account for these effects and to minimize errors, a new model was developed by Cai *et al.* [45] (Figure 4.2). The setup is similar to the Balandin *et al.* model; however, a radially symmetric hole with a radius R was used to suspend the material under investigation. Additionally, a hole was bored through the substrate so that the transmitted power could be directly measured, and consequently, the absorbed power could be determined.

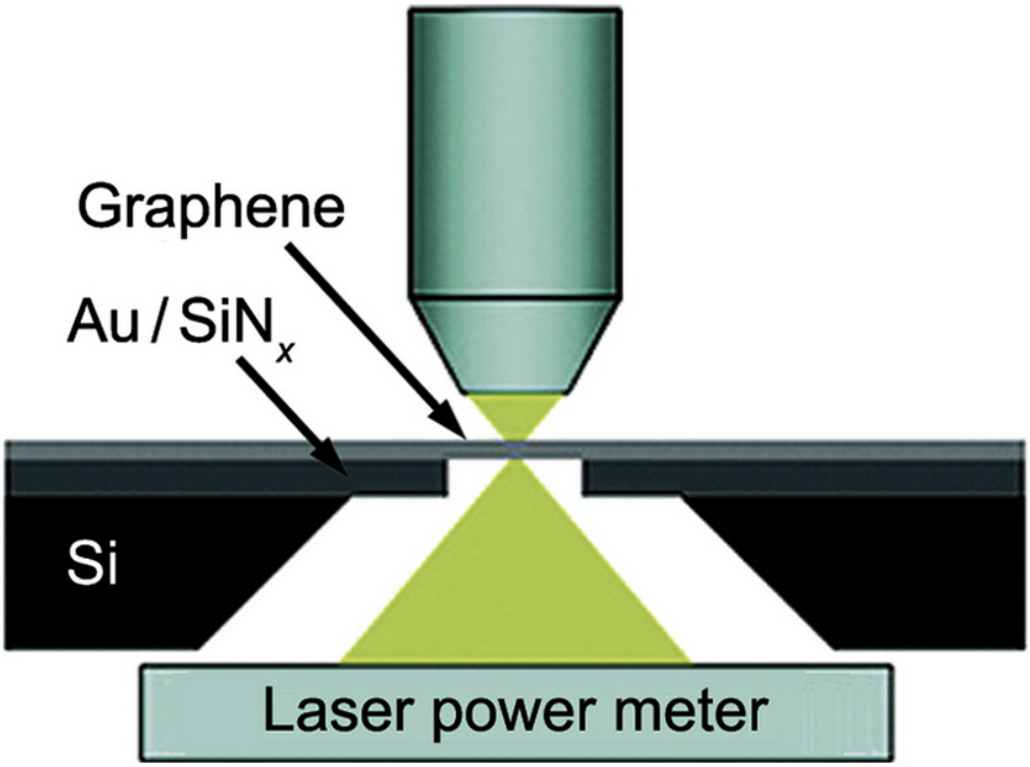

Figure 4.2: Schematic of adapted setup by Cai *et al.* to measure the power dependence Raman peak shifts over a radially symmetric hole [45].

This model also facilitated an updated description of Fourier's law, accounting for thermal boundary effects and interfacial effects of the supported region as a means to solve for a temperature profile of the suspended region ($T_1(r)$) and supported region ($T_2(r)$)

$$\kappa \frac{d}{dr}\left[r\frac{dT_1(r)}{dr}\right] + q(r) = 0 \quad ; \quad r < R \tag{4.3}$$

$$\kappa_s \frac{1}{r}\frac{d}{dr} r \frac{dT_2(r)}{dr} - \frac{g}{t}(T_2(r) - T(a)) = 0 \quad ; \quad r > R \tag{4.4}$$

Here κ is the thermal conductivity of the suspended region, κ_s is the thermal conductivity of the supported region, $q(r)$ is the volumetric power density, g is the interfacial thermal conductance between the sample and the substrate, R is the hole radius, and $T(a)$ is the ambient temperature. The general solutions are given by

$$T_1(r) = c_1 + c_2 ln(r) + c_3 Ei\Big(\frac{-r^2}{r_0^2}\Big) \quad ; \quad r < R \tag{4.5}$$

$$T_2(\gamma) = c_4 I_0(\gamma) + c_5 K_0(\gamma) + T(a) \quad ; \quad r > R \tag{4.6}$$

where c_i's are constants where $c_4 = 0$ for converging solutions, $Ei(r)$ is an exponential integral, $I_0(\gamma)$ and $K_0(\gamma)$ are zero-order modified Bessel functions (Appexdix A), r_0 is the laser spot size, and $\gamma = r\Big(g/\kappa' t\Big)^{1/2}$. The appropriate boundary conditions are given by

$$T_2(r \to \infty) = T(a) \tag{4.7}$$

$$T_1(R) = T_2(R) \tag{4.8}$$

$$-\kappa \frac{dT_1(r)}{dr}\Big|_{r=R} = -\kappa_s \frac{dT_1(r)}{dr}\Big|_{r=R} \tag{4.9}$$

$$-2\pi R t \kappa_s \frac{dT_2(r)}{dr}\Big|_{r=R} = Q \tag{4.10}$$

Here, Q is the total absorbed laser power given the difference in the power transmitted

through the empty hole and that of the suspended material, $Q = P_{empty} - P_{material}$. The measured temperature distribution (T_m) weighted by the Gaussian profile of the laser spot is given by

$$T_m \approx \frac{\int_0^R T_1(r)q(r)rdr}{\int_0^R q(r)rdr} \tag{4.11}$$

Here, T_m is solved by applying equation (4.5).

$$T_m = c_1 + c_2 a + c_3 b \tag{4.12}$$

The constants a and b are independent of laser power (Appendix A). The final result of κ is related to the total thermal resistance given by

$$\frac{\partial T_m}{\partial P} = \frac{\chi_P}{\chi_T} = \alpha\Big[\frac{2ln(R) - Ei\Big(-\frac{R^2}{r_0^2}\Big) - 2a + b}{4\pi\kappa t} + \frac{K_0(\gamma_R)}{2\pi R\sqrt{g\kappa_s t}K_1(\gamma_R)}\Big] \tag{4.13}$$

The experimentally measured values of the slopes, χ_P/χ_T are plotted against κ where the thermal conductivity is extrapolated from the independent variable axis.

4.2 Linkam Temperature Stage Setup

The setup for measuring the temperature dependence of the Raman peaks (χ_T) is depicted in Figure 4.3. This equipment consists of a hot/cold cell positioned directly beneath the laser line, connected to an inVia Renishaw Raman Spectrometer where the sample is focused. The sample on a SiO_2 substrate is placed in contact on top of the sample stage. The sample chamber is then sealed and evacuated to prevent condensation from forming on the sample during the cooling process. To regulate the temperature, liquid nitrogen is circulated through the stainless steel line connected to the sample stage. Any evaporated nitrogen is directed through a tube

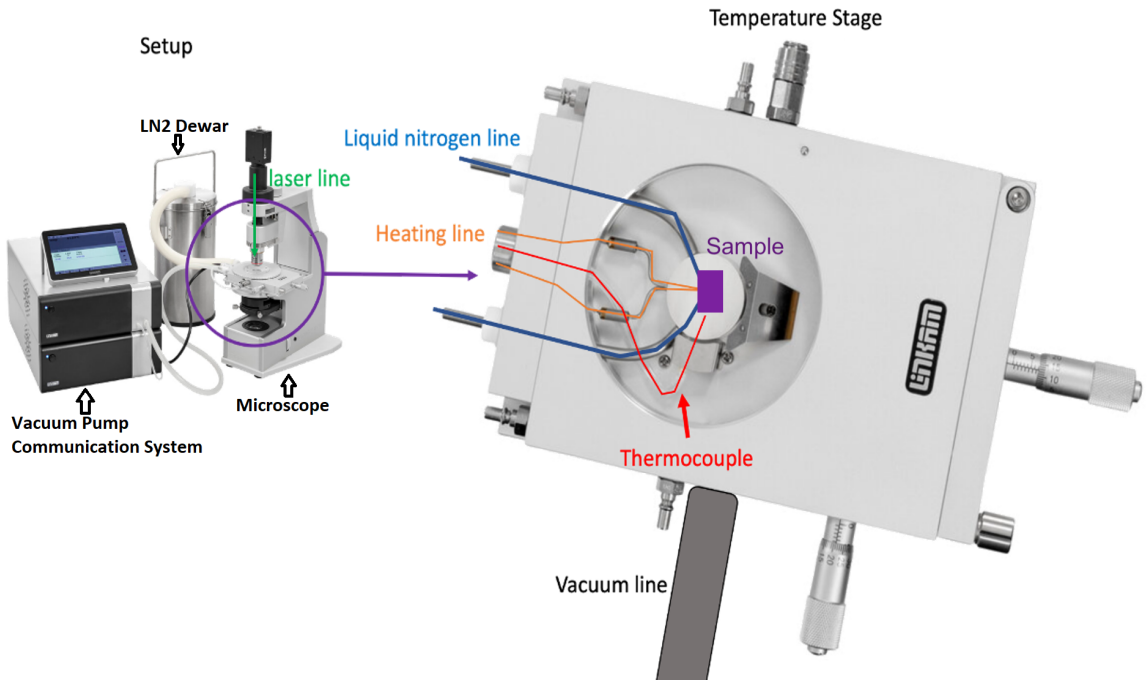

Figure 4.3: The Linkam temperature stage setup for low-temperature Raman spectroscopy.

to remove condensation on the glass window. A thermocouple is employed directly beneath the sample stage to measure the sample's temperature. The thermocouple is connected in a feedback loop to the liquid nitrogen pump, and the latter determines the correct liquid nitrogen flow rate for maintaining the desired sample temperature. Furthermore, a heating element is located directly beneath the stage to regulate temperature. The desired cooling/heating rate, set point temperature, and hold time are inputs on the controller, which then regulates the necessary steps to achieve and maintain the desired sample temperature conditions. In the current setup, the sample's temperature can be varied from -196°C to 120°C; however, some commercial stages are capable of up to 600°C.

4.3 Preliminary CVD Graphene Standard Reference Measurement

The OTR method was calibrated for a sample of graphene grown via chemical vapor deposition (CVD) synthesis to check the validity of our system and analysis. First, the CVD graphene is suspended over a 5 μm radially symmetric hole. First, the temperature dependence (χ_T) of the graphene G-band was measured (Figure 4.4) by externally varying the sample temperature using the Linkam stage. Secondly,

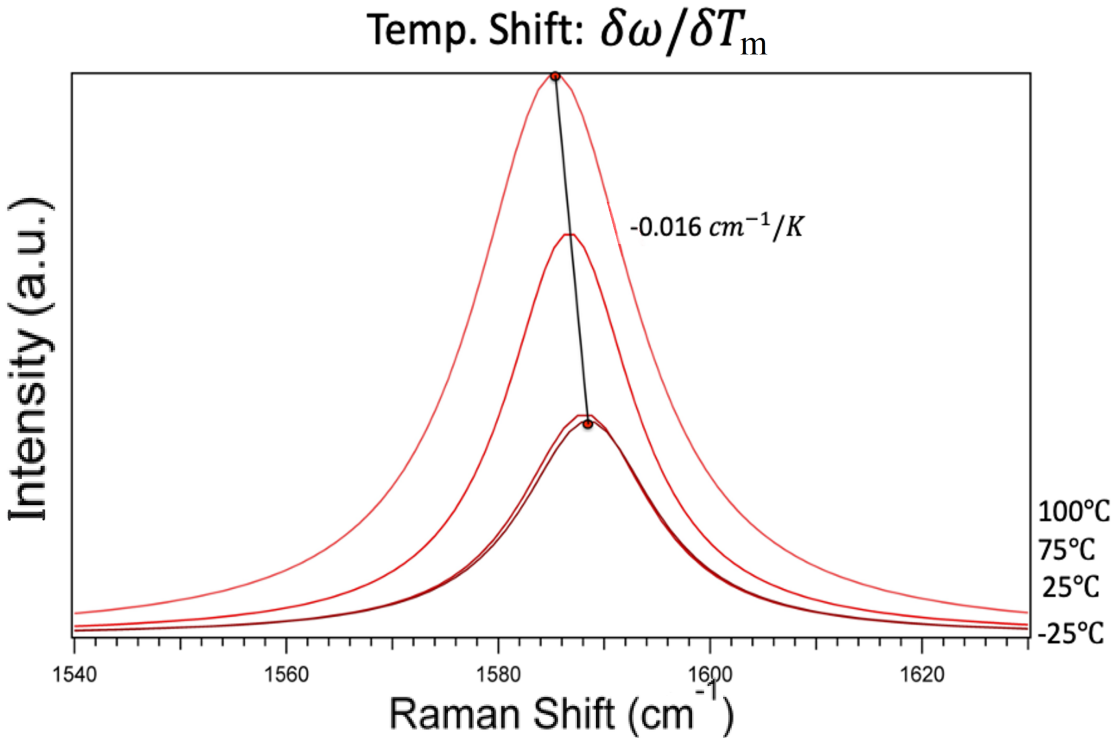

Figure 4.4: Measured G-band temperature dependence for suspended CVD graphene.

the dependence of the G-band on the incident laser power was measured, as shown in Figure 4.5. To extrapolate thermal conductivity, the experimentally determined values of $\chi_T = -0.061$ cm^{-1}/K and $\chi_P = -0.43$ cm^{-1}/mW were applied to equation

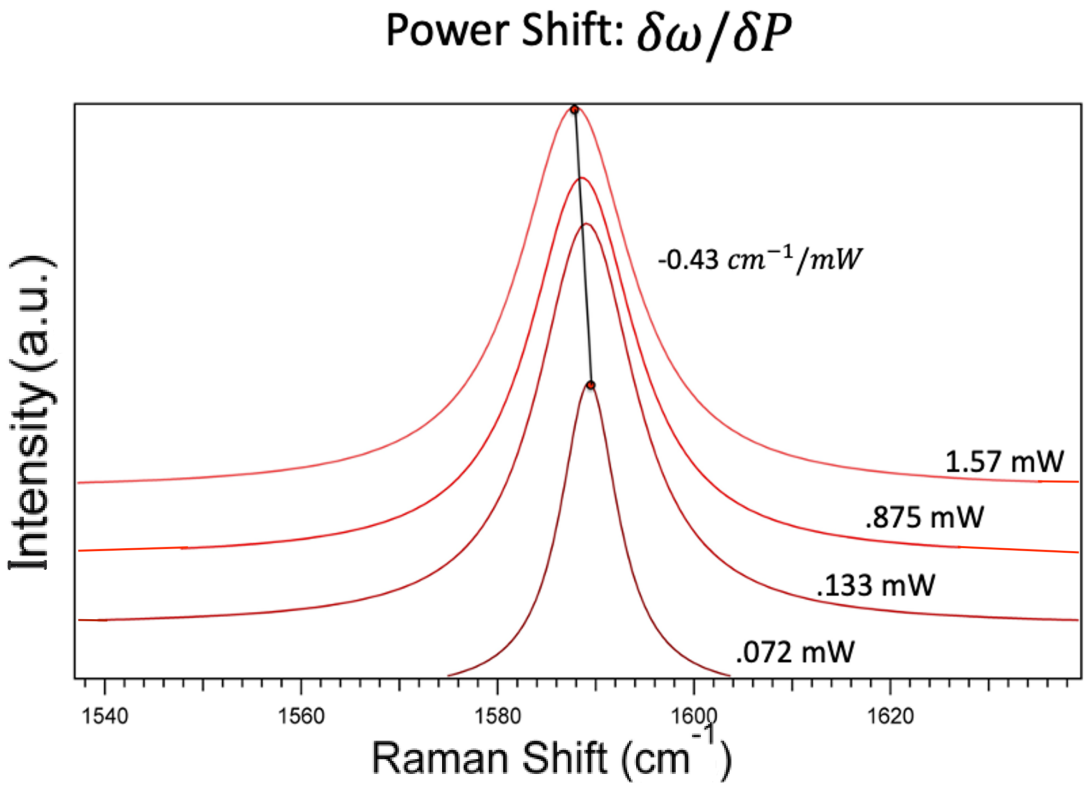

Figure 4.5: Measured G-band laser power dependence for suspended CVD graphene.

4.13. The theoretical curve was constructed using measured and literature values: $\alpha \approx 3.5$ % [45], $t = 0.335$ nm, $R = 5$ μm, $r_0 = 0.3$ μm, $\kappa_s = 600$W/m·K [45], and $g = 28$ MW/m^{2}K [45] (Figure 4.6). The extrapolated thermal conductivity was ~2000 W/m·K at room temperature. This is within the uncertainty of the literature-reported value of ~2500 (+1100 /-1050) W/m·K [45].

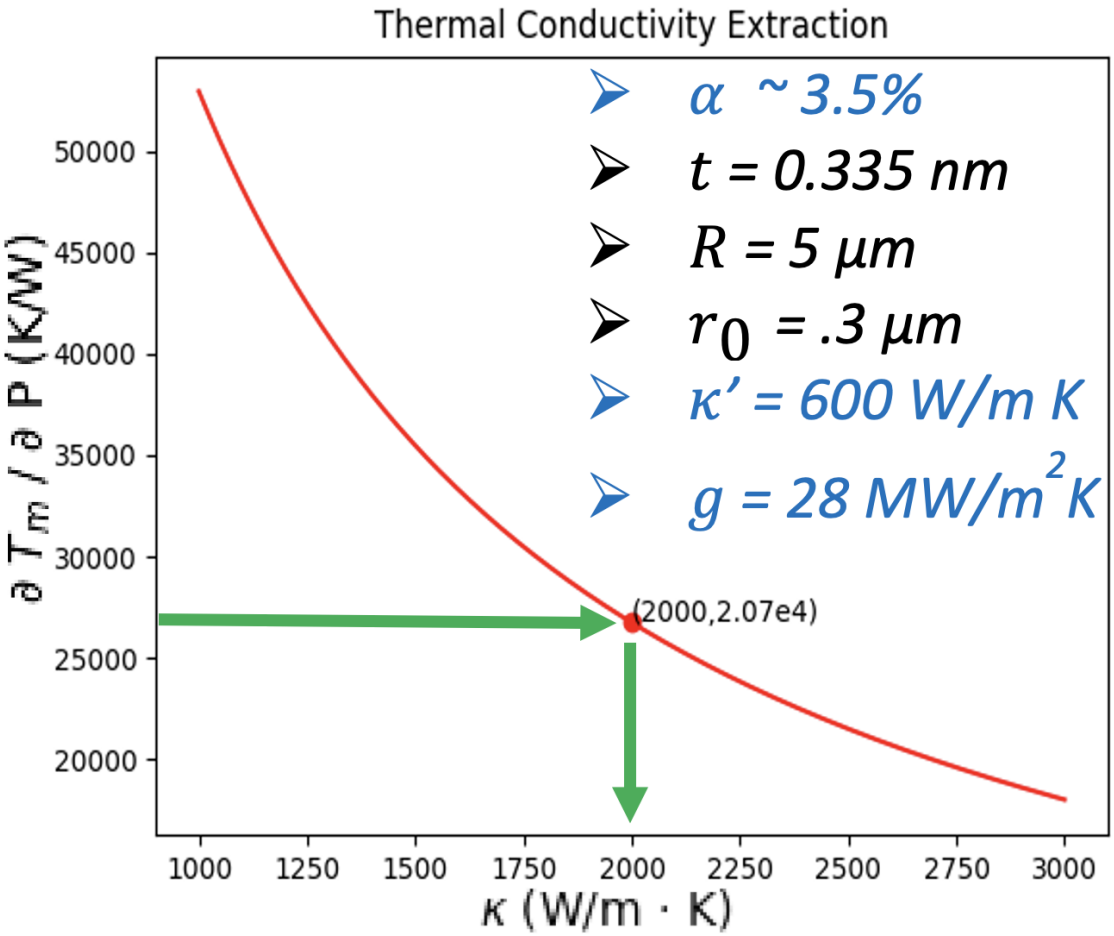

Figure 4.6: Extrapolated thermal conductivity of suspended CVD graphene, κ ~2000 W/m·K. Blue text indicates literature values from Ref [45].

4.4 OTR Method in the Macro-Configuration: Application to Optical Fibers

A prospective application of the OTR method for measuring the thermal conductivity of optical fibers is discussed. The OTR technique was first used at the macro-scale to measure the thermal conductivity of graphene laminate (GL)-on-polyethylene terephthalate (PET) with thickness varying from ~9 μm to 44 μm

[46]. Cladded fibers ($\sim$ 150 μm) are thicker than these dimensions but can be cut within this range, where an alteration of the OTR analysis can be applied. The same temperature- and power-dependent Raman peak shift measurements are performed to determine the thermal conductivity of these materials. However, there are a few key differences from the OTR analysis due to the substantial increase in the thickness of cladded optical fibers. First, higher laser power is needed to cause a sufficient local temperature rise, where the power can be upwards of 10 mW [46]. Secondly, due to the distribution of laser power in three dimensions (3D), thermal conductivity is extracted by solving heat diffusion in a 3D geometry. This requires a model of laser-induced heating where a spherical distribution of the laser power $P(x, y, z)$ through a given layer is approximated as

$$P(x, y, z) = \frac{P_{total}}{2\pi d\sigma^2} \exp -\frac{x^2 + y^2}{2\sigma^2} \exp -\frac{z}{d} \tag{4.14}$$

Here, d is the laser penetration depth, which can be determined from the dependent refractive index of the material [39, 47]. Additionally, P_{total} is the total laser power and σ is the standard deviation of the Gaussian function determined from the laser spot size. To extract thermal conductivity, the modeled differential equation is solved iteratively, where total power and thermal conductivity are the inputs to the thermal diffusion equations, which determine the temperature distribution by simulating it for different values of the experimentally determined slope. This is more easily achieved by introducing the slope parameter.

$$\Theta = \frac{\partial \omega}{\partial P} = \chi_T \frac{\partial T}{\partial P} \tag{4.15}$$

This slope parameter helps simulate the plot κ vs. Θ (Figure 4.7). The specific experimental value of the slope determines the thermal conductivity. This expansion

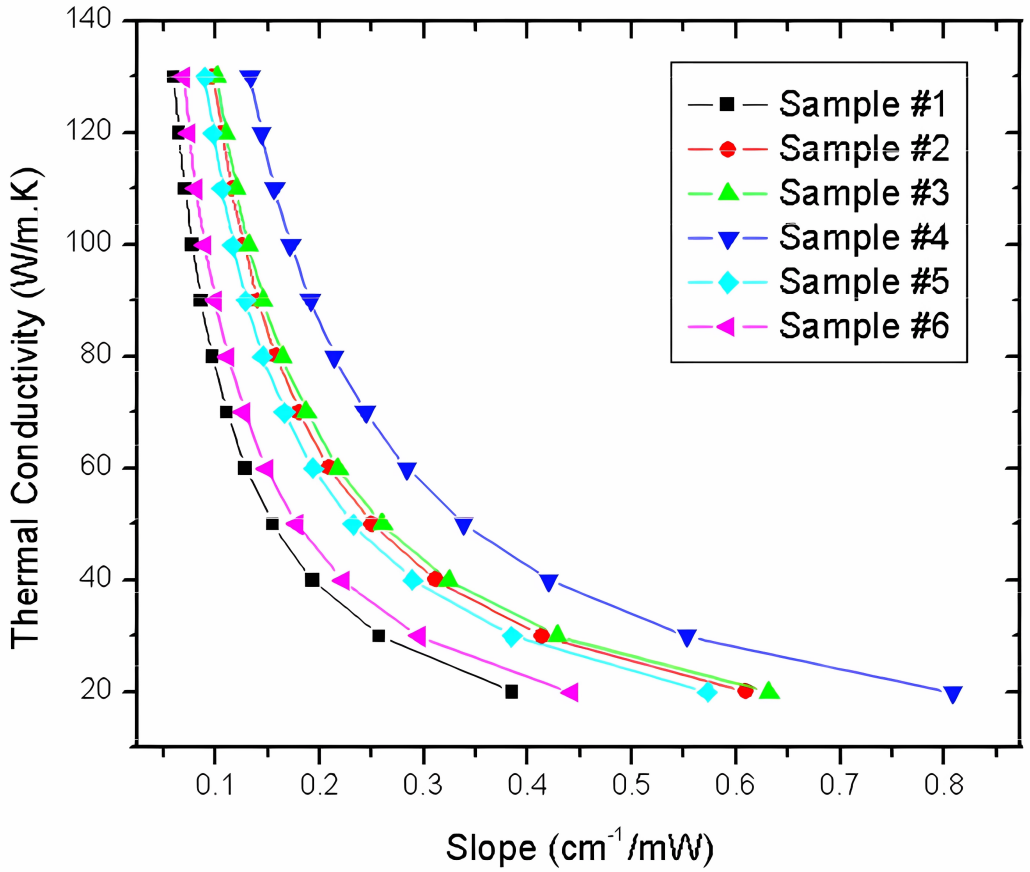

Figure 4.7: Example of thermal conductivity (κ) vs. slope parameter (Θ) for various sample thickness of GL-PET. Adapted from Ref [46].

of the OTR technique to the macroscale samples can help facilitate the determination of radial heat flow in cladded optical fiber systems, which has not been achieved to date. Additionally, it is a valuable comparison to other established methods, such as the previously discussed PTC technique.

Appendices

Appendix A Optothermal Raman Mathematical Values

Boundary conditions are used to solve for c_i's:

$$c_1 = \frac{Q\Big[2ln(R) - Ei\Big(-\frac{R^2}{r_0^2}\Big)\Big]}{4\pi\kappa t} + \frac{QK_0(\gamma_R)}{2\pi R\sqrt{g\kappa_s t}K_1(\gamma_R)} + T(a)$$

$$c_2 = \frac{-Q}{2\pi\kappa t}$$

$$c_3 = \frac{Q}{4\pi\kappa t}$$

$$c_4 = 0$$

$$c_5 = \frac{Q}{2\pi R\sqrt{g\kappa_s t}K_1(\gamma_R)}$$

Note the appropriate integrals:

$$Ei(x) = -\int_{-x}^{\infty} \frac{e^{-t}}{t} dt$$

$$I_0(\gamma) = \sum_{k=0}^{\infty} = \frac{\Big(\frac{1}{4}\gamma^2\Big)^k}{(k!)^2}$$

$$K_0(\gamma) = \int_0^{\infty} \frac{\cos(\gamma t)}{\sqrt{t^2+1}} dt$$

Constants:

$$a = \frac{\int_0^{\infty} ln(r) exp\Big(-\frac{r^2}{r_0^2}\Big) r dr}{\int_0^{\infty} exp\Big(-\frac{r^2}{r_0^2}\Big) r dr}$$

$$b = \frac{\int_0^{\infty} Ei\Big(-\frac{r^2}{r_0^2}\Big) exp\Big(-\frac{r^2}{r_0^2}\Big) r dr}{\int_0^{\infty} exp\Big(-\frac{r^2}{r_0^2}\Big) r dr}$$

References

(1) Koester, C. J.; Snitzer, E. *Applied optics* **1964**, *3*, 1182–1186.

(2) Kaushal, H.; Kaddoum, G. *IEEE Access* **2017**, *5*, 20736–20753.

(3) Dragic, P. D.; Cavillon, M.; Ballato, J. *Applied Physics Reviews* **2018**, *5*.

(4) Zervas, M. N.; Codemard, C. A. *IEEE Journal of selected topics in Quantum Electronics* **2014**, *20*, 219–241.

(5) Richardson, D. J.; Nilsson, J.; Clarkson, W. A. *JOSA B* **2010**, *27*, B63–B92.

(6) Dawson, J. W.; Messerly, M. J.; Heebner, J. E.; Pax, P. H.; Sridharan, A. K.; Bullington, A. L.; Beach, R. J.; Siders, C. W.; Barty, C.; Dubinskii, M. In *Laser Technology for Defense and Security VI*, 2010; Vol. 7686, pp 221–232.

(7) Petermann, K.; Fagundes-Peters, D.; Johannsen, J.; Mond, M.; Peters, V.; Romero, J.; Kutovoi, S.; Speiser, J.; Giesen, A. *Journal of crystal growth* **2005**, *275*, 135–1.

(8) Marchese, S. V.; Baer, C. R.; Peters, R.; Kränkel, C.; Engqvist, A.; Golling, M.; Maas, D.; Petermann, K.; Südmeyer, T.; Huber, G., et al. *Optics express* **2007**, *15*, 16966–16971.

(9) Dong, L.; Ballato, J.; Kolis, J. *Optics Express* **2023**, *31*, 6690–6703.

(10) McMillen, C.; Thompson, D.; Tritt, T.; Kolis, J. *Crystal growth & design* **2011**, *11*, 4386–4391.

(11) Hufner, S., *Optical spectra of transparent rare earth compounds*; Elsevier: 2012.

(12) Kojima, N.; Tsushima, K.; Tsujikawa, I. *Journal of the Physical Society of Japan* **1980**, *49*, 1449–1455.

(13) Liu, Z.; Ikesue, A.; Li, J. *Journal of the European Ceramic Society* **2021**, *41*, 3895–3910.

(14) Novak, J. Diode pumped thin disk lasers for high repetition rate picosecond OPCPA pumping, Ph.D. Thesis, Czech Technical University, 2016.

(15) Kuznetsov, M.; Antipov, O.; Fotiadi, A.; Mégret, P. *Optics Express* **2013**, *21*, 22374–22388.

(16) Zawilski, B. M.; Littleton IV, R. T.; Tritt, T. M. *Review of Scientific Instruments* **2001**, *72*, 1770–1774.

(17) Murgatroyd, J. *J Soc Glass Technol* **1944**, *28*, 368–387.

(18) Matthewson, M. J.; Kurkjian, C. R.; Gulati, S. T. *Journal of the American Ceramic Society* **1986**, *69*, 815–821.

(19) Timoshenko, S., *Theory of elasticity*; Oxford: 1951.

(20) Brook, R. J., *Concise encyclopedia of advanced ceramic materials*; Elsevier: 2012.

(21) Cahill, D. G. *Review of scientific instruments* **1990**, *61*, 802–808.

(22) Filler, R.; Lindenfeld, P.; Deutscher, G. *Review of Scientific Instruments* **1975**, *46*, 439–442.

(23) Tang, X.; Aaron, K.; He, J.; Tritt, T. M. *physica status solidi (a)* **2008**, *205*, 1152–1156.

(24) Aaron, K. R. Measurement of the In-Plane Thermal Conductivity of Single Crystals by the Modified Parallel Thermal Conductance Technique, 2005.

(25) Lesker, K. J. KJLC 979 Series Wide-Range Combination Gauges `https://www.lesker.com/newweb/gauges/widerange_kjlc_979.cfm`.

(26) Tuttle, J.; Canavan, E.; DiPirro, M. In *AIP Conference Proceedings*, 2010; Vol. 1219, pp 55–62.

(27) Zavaritskii, N. *Zhur. Tekh. Fiz.* **1956**, *26*, 2032.

(28) AZO Phosphor Bronze – Copper Alloy UNS C52100 `https://www.azom.com/article.aspx?ArticleID=6417`.

(29) Concast C51000 `https://www.concast.com/c51000.php`.

(30) MatWeb Phosphor bronze 10% Sn, UNS C52400, H02 Temper flat products `https://www.matweb.com/search/datasheet.aspx?MatGUID=ee11f0e84c8e4e3893beac2ab2e8ebbe&ckck=1`.

(31) MatWeb Phosphor bronze 8% Sn, UNS C52100, H08 Temper flat products `https://www.matweb.com/searh/datasheet.aspx?matguid=ad6c1f78e59a43e1a67f001392dcba50&n=11`.

(32) Mezhov-Deglin, L. *Zh. Eksp. Teor. Fiz.* **1965**, *49*, 66.

(33) Kittel, C., *Introduction to solid state physics*; John Wiley & sons, inc: 2005.

(34) Lee, S.; Broido, D.; Esfarjani, K.; Chen, G. *Nature communications* **2015**, *6*, 6290.

(35) Bhattacharya, S.; Dehkordi, A. M.; Alshareef, H. N.; Tritt, T. *Journal of Physics D: Applied Physics* **2014**, *47*, 385302.

(36) Balandin, A. A.; Ghosh, S.; Bao, W.; Calizo, I.; Teweldebrhan, D.; Miao, F.; Lau, C. N. *Nano letters* **2008**, *8*, 902–907.

(37) Calizo, I.; Balandin, A.; Bao, W.; Miao, F.; Lau, C. *Nano letters* **2007**, *7*, 2645–2649.

(38) Ghosh, D.; Calizo, I.; Teweldebrhan, D.; Pokatilov, E. P.; Nika, D. L.; Balandin, A. A.; Bao, W.; Miao, F.; Lau, C. N. *Applied Physics Letters* **2008**, *92*, 151911.

(39) Malekpour, H.; Balandin, A. A. *arXiv preprint arXiv:1710.09749* **2017**.

(40) Malekpour, H.; Ramnani, P.; Srinivasan, S.; Balasubramanian, G.; Nika, D. L.; Mulchandani, A.; Lake, R. K.; Balandin, A. A. *Nanoscale* **2016**, *8*, 14608–14616.

(41) Yan, R.; Simpson, J. R.; Bertolazzi, S.; Brivio, J.; Watson, M.; Wu, X.; Kis, A.; Luo, T.; Hight Walker, A. R.; Xing, H. G. *ACS nano* **2014**, *8*, 986–993.

(42) Zhang, X.; Sun, D.; Li, Y.; Lee, G.-H.; Cui, X.; Chenet, D.; You, Y.; Heinz, T. F.; Hone, J. C. *ACS applied materials & interfaces* **2015**, *7*, 25923–25929.

(43) Zou, B.; Zhou, Y.; Zhang, X.; Zhang, M.; Liu, K.; Gong, M.; Sun, H. *ACS Applied Nano Materials* **2020**, *3*, 10543–10550.

(44) Beechem, T.; Yates, L.; Graham, S. *Review of Scientific Instruments* **2015**, *86*, 041101.

(45) Cai, W.; Moore, A. L.; Zhu, Y.; Li, X.; Chen, S.; Shi, L.; Ruoff, R. S. *Nano letters* **2010**, *10*, 1645–1651.

(46) Malekpour, H.; Chang, K.-H.; Chen, J.-C.; Lu, C.-Y.; Nika, D.; Novoselov, K.; Balandin, A. *Nano letters* **2014**, *14*, 5155–5161.

(47) Ni, Z.; Wang, Y.; Yu, T.; Shen, Z. *Nano Research* **2008**, *1*, 273–291.